1

1

Revision 2

Experimentally-derived F, Cl, and Br fluid/melt partitioning of

intermediate to silicic melts in shallow magmatic systems

Mike Cassidy,[1]* Alexander A. Iveson, [2] Madeleine C.S. Humphreys,[2] Tamsin A.

Mather,[1] Christoph Helo,[3] Jonathan M. Castro[3], Philipp Ruprecht[4], David M. Pyle[1], and

EIMF[5]

[1]Department of Earth Sciences, University of Oxford, U.K.

[2]Department of Earth Science, University of Durham, U.K.

[3]Institute for Geoscience, Johannes Gutenberg University of Mainz, Germany

[4]Department of Geological Sciences and Engineering, University of Nevada, Reno, U.S.A.

[5]Edinburgh Ion Microprobe Facility, U.K.

*Corresponding author: michael.cassidy@earth.ox.ac.uk

ABSTRACT

The conditions under which halogens partition in favour of an exsolved fluid relative to the

coexisting melt are key for understanding many magmatic processes, including volcanic

degassing, evolution of crustal melt bodies, and ore formation. We report new F, Cl and Br

fluid/melt partition coefficients for intermediate to silicic melts, for which F and Br data are

particularly lacking; and for varying CO_2-H_2O contents to assess the effects of changing fluid

composition (XH_2O) on Br fluid/melt partitioning for the first time. The experiments were

conducted at pressures 50-120 MPa, temperatures 800–1100°C and volatile compositions

(molar XH_2O = $H_2O/(H_2O + CO_2)$) of 0.55 to 1, with redox conditions around the Nickel-

25   Nickel Oxygen buffer ($fO_2 \approx$ NNO). Experiments were not doped with Cl, Br or F and were

26   conducted on natural crystal-bearing volcanic products at conditions close to their respective

27   pre-eruptive state. The experiments therefore provide realistic constraints on halogen

28   partitioning at naturally occurring, brine-undersaturated conditions. Measurements of Br, Cl

29   and F were made by Secondary Ion Mass Spectrometry (SIMS) on thirteen experimental

30   glass products spanning andesite to rhyolitic compositions, together with their natural starting

31   materials from Kelud volcano, Indonesia, and Quizapu volcano, Chile. Fluid compositions

32   were constrained by mass balance. Average bulk halogen fluid/melt partition coefficients and

33   standard deviations are: $D_{Cl}^{fluid/melt}$ = 3.4 ($\pm$ 3.7 1 s.d.) $D_F^{fluid/melt}$ = 1.7 ($\pm$ 1.7) and $D_{Br}^{fluid/melt}$ =

34   7.1 ($\pm$ 6.4) for the Kelud starting material (bulk basaltic andesite), and $D_{Cl}^{fluid/melt}$ = 11.1 ($\pm$

35   3.5), $D_F^{fluid/melt}$ = 0.8 ($\pm$ 0.8) and $D_{Br}^{fluid/melt}$ = 31.3 ($\pm$ 20.9) for Quizapu starting material (bulk

36   dacite). The large range in average partition coefficients is a product of changing XH_2O,

37   pressure and temperature. In agreement with studies on synthetic melts, our data show an

38   exponential increase of halogen $D^{fluid/melt}$ with increasing ionic radius, with partitioning

39   behaviour controlled by melt composition according to the nature of the complexes forming

40   in the melt (e.g., SiF_4, NaCl, KBr). The fundamental chemistry of the different halogens

41   (differing ionic size and electronegativities) controls the way in which partitioning responds

42   to changes in melt composition, and other variables. Experimental results confirm that more

43   Cl partitions into the fluid at higher bulk Cl contents, higher melt Na, higher fluid XH_2O

44   ratios and lower temperatures. Bromine shows similar behaviour, though seems to be more

45   sensitive to temperature, and less sensitive to Na content and XH_2O. In contrast, F

46   partitioning into the fluid increases as the melt silica content decreases (from 72 to 56 wt%

47   SiO_2), which we attribute to the lower abundance of Si available to form F complexes in the

48   melt. These new data provide more insights into the conditions and processes that control

49 halogen degassing from magmas, and may help to inform the collection and interpretation of

50 melt inclusions and volcano gas data.

51

52 **INTRODUCTION**

53   Halogen behaviour in magmas impacts a range of crustal processes, including magma

54 evolution, degassing and ore mineralisation, by influencing the physical and chemical

55 properties of melts, fluids and minerals (Aiuppa et al. 2009; Pyle and Mather 2009; Bodnar et

56 al. 2013; Harlov and Aranovich 2018; Webster et al. 2018). Although halogens may partition

57 into crystals, gases and brine phases, this study concentrates on partitioning of halogens

58 between the melt and aqueous fluid phase. Much previous work has concentrated on Cl, due

59 to its ease of measurement in glasses by electron microprobe; and substantial advances in our

60 understanding of Cl behaviour in melts can be attributed to J.D. Webster. Chlorine fluid/melt

61 partitioning ($D_{Cl}^{fluid/melt}$) behaviour has been quantified for a range of silicate melt

62 compositions (Webster and Holloway 1990; Webster 1997; Webster et al. 2014), pressures

63 (Alletti et al. 2009; Botcharnikov et al. 2015; Webster et al. 2017), temperatures (Stelling et

64 al. 2008), fO_2 (Beermann et al. 2015), and volatile contents (Lowenstern 1994; Botcharnikov

65 et al. 2006; Alletti et al. 2009; Webster et al. 2014; Hsu et al. 2019). Fluorine, a relatively

66 difficult element to measure in silicate glass (due to elemental interferences on the electron

67 microprobe), has received less study, with most experiments focusing on end-member silicic

68 or alkaline magmas (figure 1) (Webster and Holloway 1990; Borodulin et al. 2009; Iveson et

69 al. 2017) and few data available for mafic and intermediate magmas (Chevychelov et al.

70 2008). Likewise, there are few data for bromine (figure 1) (Bureau et al. 2000; Bureau et al.,

71 2010; Cadoux et al. 2018) because of its low abundance and analytical challenges.

72 Nonetheless, the behaviour of bromine is of interest for its potential atmospheric impacts and

4

73   detection of BrO in volcanic plumes by remote sensing (Aiuppa et al. 2005; Pyle and Mather

74   2009; Donovan et al. 2014; Gutmann et al. 2018).

75   The strong electronegativity of halogens largely controls their behaviour in magmas, and

76   explains their propensity to form strong bonds, often with a high degree of polar or ionic

77   character. The differing electronegativities and ionic radii of the halogens lead to element-

78   specific effects in melts and fluids (Dolejš and Zajacz 2018; Webster et al. 2018). For

79   instance, the high electronegativity of F (relative to Cl and Br) promotes strong interactions

80   with cations in silicate melts, enhancing its solubility in melts and thus lowering its degassing

81   potential compared to the other halogens (Webster et al., 2018). During crystallisation of

82   magmas the relatively small F^- ion (1.33 Å) also substitutes effectively for similarly sized, O^{2-}

83   (1.26 Å) and OH^- (1.32-1.37 Å) within the melt and is therefore thought to partition into

84   silicate melts during volatile-undersaturated magma differentiation (e.g., Dolejš & Baker,

85   2007; Webster, 1990). In contrast, Cl and Br are thought to become less enriched in the melt

86   during differentiation, as they partition to a fluid phase as melts become more silicic. Their

87   larger ionic masses and radii, Cl^- (1.81 Å) and Br^- (1.95 Å) and the greater mismatch

88   compared to O^{2-} and OH^- make Cl and Br less likely to be incorporated into the

89   aluminosilicate network (Bureau et al., 2000) and promote a higher affinity with a coexisting

90   aqueous fluid phase (Bureau et al. 2000; Bureau and Métrich 2003). Thus, Cl and Br

91   fractionate more strongly into coexisting fluid during magmatic degassing compared with the

92   lighter and smaller F (Teiber et al. 2014). Furthermore, the larger lattice energies for fluorides

93   and higher hardness/bond strength as a ligand for complexing in comparison to chlorides,

94   means a preference of F for the melt, and also the higher solubility of chlorides in aqueous

95   fluids (Webster et al. 2015; Dolejš and Zajacz 2018).

96   The influence of melt composition on halogen behaviour is a product of the complexes they

97   form with the cations in the melt. Chlorine dominantly dissolves in the melt by complexation

98 with network modifying alkaline earth metals (Mg, Ca), alkalis (Na, K) and also Al and Fe,

99 whereas it dissolves as an HCl species in aqueous magmatic fluids (Webster 1997; Webster

100 and De Vivo 2002; Thomas and Wood 2020). Conversely, it is thought that F occurs in

101 silicate melts as Si-F, Al-F, Na-F and Ca-F complexes (Dalou and Mysen 2015; Dalou et al.

102 2015; Bell and Simon 2011), while Br forms NaBr complexes at high pressure (>2 GPa) in

103 hydrous felsic melts (Cochain et al. 2015; Louvel et al. 2020). The effect of melt composition

104 on F and Br fluid/melt partitioning is currently unclear, as few studies span intermediate to

105 silicic melt compositions (Figure 1).

106 In magmatic systems the addition of volatiles such as CO_2 is known to influence the

107 fluid/melt partitioning of chlorine: $D_{Cl}^{fluid/melt}$ decreases with increasing CO_2 addition, which

108 is thought to be related to an increase of the activity coefficient for NaCl in the fluid phase,

109 which decreases the stability of hydrated metal complexes in aqueous fluids, such as NaCl

110 ion pairs (Alletti et al., 2009; Hsu et al., 2019). The effect of CO_2 on F and Br partitioning

111 between fluid and melt is less studied, and our research assesses whether, like Cl, CO_2

112 presence in the fluid also decreases their fluid/melt partition coefficients. At low Cl

113 concentrations <2.5 wt% in basaltic melts (Webster et al., 2015), and <0.25 wt% in rhyolitic

114 melts (Zajacz et al. 2012), Cl fluid/melt partitioning exhibits Henrian behaviour where the

115 increasing Cl content of the melt varies linearly with increasing Cl in the co-existing fluid.

116 However, with increasing Cl concentrations, partitioning behaviour becomes non-linear and

117 subsolvus fluid exsolution yields a lower density aqueous phase and a higher density

118 hydrosaline brine (e.g., Webster et al. 1999; Shinohara 2009). We concentrate here on brine-

119 undersaturated conditions, where halogen partitioning should follow Henrian behaviour and

120 thus be more constant (Baker and Alletti, 2012). These conditions apply to the many active

121 magmatic systems that have low halogen concentrations (Aiuppa et al. 2009) and lack a

122 separate brine phase (Baker and Alletti 2012).

123   Recent experimental work by Thomas and Wood (2020) provides new insights into the

124   chemical and thermodynamic basis for chlorine dissolution in silicate melts. The initial Cl

125   dissolution into the melt involves the replacement of O^{2-} by two dissociated Cl^- ions:

126   $Cl_2^{fluid} + [O^{2-}]^{melt} = 2[Cl^-]^{melt} + 0.5O_2^{fluid\ or\ melt}$
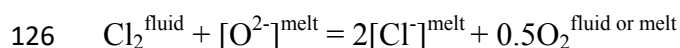
127   This leads to a formulation for chlorine solubility in anhydrous basalts (Thomas & Wood

128   2020):

129   $Log(Cl^{melt}) = 0.984(64) - 930(70)P/T - 0.25log(fO_2) + 0.5log(fCl_2)$.

130   Where P is in GPa, T in K, and fO_2 and fCl_2 refer to the fugacities of a pure gas at 0.1 MPa

131   and the temperature of interest. Values in brackets are 1 standard error of the last two digits

132   for the corresponding experimentally determined constants.

133   This relationship predicts that in mafic systems at fixed O_2 and Cl_2 fugacities, increasing

134   temperature should increase chlorine solubility of the melt (and therefore lower $D_{Cl}^{fluid/melt}$),

135   while increasing pressure should decrease the chlorine solubility (and thus increase

136   $D_{Cl}^{fluid/melt}$). While the relationship between $D^{fluid/melt}$ with temperature has been observed

137   experimentally for Cl and Br, behaving in the same way (Webster et al., 2015; Cadoux et al.,

138   2018), the results for F are less clear (Borodulin et al. 2009) and have been investigated in

139   this study.

140   In this study we test the theoretical and experimental hypotheses described above, i.e., the

141   role of ionic size, metal-ligand complexing, volatile composition (H_2O-CO_2) and variable

142   temperature, on fluid/melt partitioning of F, Cl and Br. In particular we present new data on

143   andesitic to rhyolitic melts to test whether i) classic phase equilibria experiments can be used

144   for halogen partitioning determination, ii) the larger Cl and Br ions behave similarly to each

145   other, preferring the fluid over the melt with the fluid preference increasing with increasing

146   ionic radius, iii) F partitions into melt during differentiation whereas Cl and Br do not and

147 instead associate with a fluid phase, iv) increasing temperature and CO_2 reduces partitioning

148 of Cl into the fluid, along with other halogens.

149

150 **METHODS**

151 **Experimental and analytical rationale**

152 The experimental and analytical approach used in this study differs in several ways from

153 previous studies. Our starting materials are deliberately tailored to specific magmatic

154 systems, with the exact compositions, including the observed crystal assemblage, and the

155 partition experiments run at pressures and temperatures which matched their pre-eruptive

156 (experimentally-constrained) conditions (First et al. 2021; Cassidy et al. 2019). Capsules

157 were not doped with added halogens. Only water ± carbon dioxide were added to reach fluid

158 saturation. This approach was chosen to reproduce as close to 'real' conditions as the

159 magmas experienced at their respective pre-eruptive storage conditions (e.g., 50-100 MPa for

160 the bulk basaltic andesite composition of Kelud and 120 MPa for the bulk dacitic

161 composition of Quizapu equating to 2-5 km depth) and to ensure pressure, temperature, and

162 X_{H2O}^{fluid}, and brine-undersaturation conditions appropriate for the stored magmas (Cassidy et

163 al. 2019; First et al. 2021). Due to the low concentrations and potential interferences,

164 measurements were made by Secondary Ion Mass Spectrometry (SIMS). Despite the different

165 experimental and analytical approach, we find encouragingly similar partitioning values

166 compared to previously published experiments using synthetic and doped natural starting

167 materials (Table S1).

168 This study focuses on two active and well-characterized systems, which are typical of

169 subduction zone magmas undergoing crustal storage and degassing, and span the

170 intermediate-silicic compositional range that is involved in the enrichment of metals and for

171   which halogen partitioning data are least abundant (figure 1; Table S1; (Tattitch et al. 2021)).

172   . Although some Cl data exist for compositions similar to Kelud and Quizapu (e.g., Zajacz et

173   al., 2012), F and Br data are lacking, along with H_2O+CO2-bearing experiments at low

174   pressures that allow us to understand their fluid/melt partitioning.

175   **Experimental procedure**

176   Natural samples of crystal-bearing basaltic-andesite from Kelud volcano and dacite from

177   Quizapu volcano (IGSN: PPRAI101F) were used as starting materials. The Kelud basaltic

178   andesite contains 50-60% crystals of plagioclase, ortho- and clinopyroxene, magnetite and

179   matrix glass of dacite composition (Cassidy et al., 2016; Jeffery et al., 2013). The Quizapu

180   dacite has a crystal content of 10-20 wt%, comprising plagioclase, amphibole, orthopyroxene,

181   subordinate clinopyroxene, and accessory phases including apatite, titanomagnetite, ilmenite,

182   sulfide blebs, and zircon, together with a mostly rhyolitic matrix glass (Ruprecht et al., 2012).

183   These samples were coarsely crushed (sub mm size) to preserve the crystal cores. The cores

184   act as nuclei, which become mantled by new crystal growth of a composition which is in

185   equilibrium with the evolved matrix melt in the experiments. This ensures a realistic

186   composition of the 'reactive melt' inside the shallow magmatic system (Pichavant et al. 2007;

187   Erdmann et al. 2016). This approach was chosen as it more closely resembles natural

188   conditions (i.e., melt, crystals and bubbles) and minimises concerns around structural changes

189   to the melt and to the system overall, potentially affecting nucleation sites and crystallization

190   kinetics, when starting from synthetic compounds or superliquidus conditions (Hammer

191   2008).

192   Approximately 0.1 g of sample was inserted into $Ag_{70}Pd_{30}$ capsules (wall thickness 0.25 mm,

193   capsule diameter is 4 mm), together with approximately 0.01 g distilled water using a micro

194   syringe, which was enough to saturate the melt in H_2O at the pressure and temperature of the

195   experiments. The fluid to rock ratio was ~0.1 for most experiments; exact fluid masses were

196   measured and used for subsequent mass balance calculations. For mixed volatile experiments

197   $AgCO_3$ powder was added in specific molar proportions along with specific quantities of

198   water (measured by mass), to generate water fractions (X_{H2O}) of 0.55 in the fluid phase

199   [molar $X_{H2O} = H_2O/(H_2O + CO_2)$]. X_{H2O} of 0.55 was chosen to provide a contrasting but

200   realistic value for comparison with pure water ($X_{H2O} = 1$) experiments. Capsules were sealed

201   closed using an arc welder.

202   Experiments below 900 °C were conducted in hydrothermal cold seal pressure vessels (using

203   Rene 41 autoclaves) at the University of Oxford, United Kingdom. For experiments

204   exceeding 900 °C, gas-pressurized cold seals constructed ofh TZM (Tungsten-Zirconium-

205   Molybdenum) alloy with argon as the pressurizing medium were used at the University of

206   Mainz, Germany. To fix the oxygen fugacity for the gas pressured TZM experiments at the

207   Nickel-Nickel-Oxygen buffer (NNO), a double-capsule technique was used, whereby Ni

208   powder was added to a platinum foil capsule and left open to equilibrate with the melt (Shea

209   & Hammer, 2013). In addition, methane was added as a reducing agent along with argon (0.4

210   MPa partial pressure), as tested in Shea and Hammer (2013). Ni metal powder (grey) oxidizes

211   to green NiO, providing an easy visual check that the buffer is not exhausted at the end of the

212   experiment. The oxidation conditions for the hydrothermal pressure vessels with Ni-Co alloy,

213   Rene 41 autoclaves, were buffered at ~NNO by pure Nickel filler rods situated next to the

214   capsule (Matthews et al., 2003).

215   A K-type thermocouple was inserted into a small hole in the end of the autoclave close to the

216   capsule position to check for temperature offset between the furnace's internal thermocouple

217   and autoclave. The samples were held at a constant pressure and temperature to replicate

218   magmatic storage conditions for the specific volcanic systems, for up to 7 days (table 1), and

219   the experiments were then rapidly quenched (<1 minute) in both cold seal and gas pressured

220   experiments with a water-cooled system. Experimental run times were varied as a function of

221   temperature, with a minimum of 25 hours for experiments at 1100 °C for basaltic andesite

222   runs, and 160+ hours for silicic compositions and temperature of 800-900 °C. These run

223   durations are similar to other partitioning studies with the shortest durations that reached

224   equilibrium in 3-4 hours for chlorine partitioning experiments in basalts at 1200 °C (Alletti et

225   al. 2009). However, Br diffusion is slower, which led Cadoux et al. (2018) to run their

226   experiments at 1200 °C for 24 hours, the minimum time used in our experiments. For silicic

227   compositions, Kravchuk and Keppler (1994) ran partitioning experiments at 800 °C, varying

228   run times between 93 and 1142 hours with little difference to measured halogen contents.

229   Capsules were weighed before and after welding and following quenching of the experiments

230   to ensure no fluid loss occurred; if mass loss was recorded, the experiments were discarded.

231   Backscattered electron imaging of the run products showed microlite-free glass (figure S1)

232   with little chemical variability (table 3).

Analytical techniques

234   **Electron microprobe analysis (EMPA)**. The starting materials and experimental

235   glasses were made into polished resin mounts (Epo thin 2) and carbon coated. They were

236   analysed for their major element compositions by electron microprobe (EMPA) using a JEOL

237   JXA 8200 superprobe at the University of Mainz and a Cameca SX-FiveFE at the University

238   of Oxford. The operating conditions were: 15 kV accelerating voltage, 6-8 nA beam current,

239   with a 10 μm defocussed beam and counting times of 50-200 s per analysis. Na and K peaks

240   were counted first and for short (15 seconds) duration to minimise migration (Nielsen and

241   Sigurdsson, 1981). Chlorine and fluorine were measured on the PETH and TAP crystals

242   respectively, at counting times of 40 seconds each. A Phi-rho-Z correction for atomic

243   number, absorption, and fluorescence was applied to all analyses, and the calibration was

244   performed using a range of natural and synthetic reference materials. One sigma standard

245 deviations were generally less than 2% for most major elements analysed. Secondary

246 reference materials were measured on both EMPA instruments to ensure consistency and to

247 assess the accuracy and precision, which can be found in table S2.

248 **Scanning Electron Microscope (SEM) image analysis**. Quantitative textural

249 analysis of the glass was conducted using backscattered electron imagery combined with

250 published energy dispersive spectrometer (EDS) mapping, from Cassidy et al. (2019).

251 Carbon-coated samples were imaged at 15 kV, a working distance of ~10 mm using a FEI

252 Quanta 650 SEM at the University of Oxford. To measure the glass content of the initial

253 starting powder and final experimental products >10 back scattered electron images of each

254 sample were taken and ~300 crystals were digitised using image processing software. The

255 glass fraction was then quantified with ImageJ and is presented in Table 2.

256

257 **Secondary ion mass spectrometry (SIMS) analysis**.

258 The polished resin mounts were gold-coated (~30 nm thickness) and analysed on a Cameca

259 IMS 1270 instrument at the NERC ion microprobe facility at the University of Edinburgh.

260 The samples were placed in a vacuum to outgas for >14 hours prior to analyses. Vacuum in

261 the main chamber during analysis was $<5 \times 10^{-8}$ Torr.

262 Halogen analyses were performed in two different sessions, both using a 10 kV, Cs+ primary

263 ion beam of ~2 nA for Cl and F, and ~7 nA for Br, with the normal incidence electron flood

264 gun for charge neutralisation and the electron multiplier (EM0) as the secondary ion detector.

265 After pre-sputtering for 60 s, the magnet calibration was checked and the automated

266 secondary beam alignment adjusted using either ^{18}O or $^{30}Si^{16}O_3$ as the reference peak.

267 For F and Cl analysis ^{18}O, ^{19}F, ^{30}Si and ^{35}Cl were measured at a mass resolution of 3,200, an

268 energy window of 60 eV, an analysed region of ~7 × 10 μm and magnetic peak switching.

269 Each analysis consisted of 10 cycles, in which ^{28}Si and ^{18}O were counted for 2 s each and ^{19}F

270 and ^{35}Cl for 4 s each. The secondary ion beam intensity measured at masses ^{19}F and ^{35}Cl were

271 normalized to ^{18}O. To calculate the sample composition, we used MPI-DING reference

272 glasses (StHs80, ML-3BG, T1G, ATHO-G, Jochum et al. 2006) and the USGS reference

273 glass BCR-2G. The fluorine concentration of the unknown sample was given by:

274 $$F_{concentration} = \left[\frac{^{19}F(cps)}{^{18}O(cps)} \right] * Re\,lative\,Ion\,Yield$$

275 Where the cps refers to counts per second, Relative Ion Yield = (Ion Yield F/ Ion Yield O)

276 averaged over multiple primary standards, and

277 Ion Yield F = ^{19}F (cps)/known F concentration

278 Ion Yield O = ^{18}O (cps)/known O concentration

279 Chlorine concentrations were given by similar equations for the ^{35}Cl count rate (cps)

280 normalized to the ^{18}O count rate (cps).

281 The standard deviation of the primary standard calibration of the Relative Ion Yields for F

282 and Cl were lower than 4%.

283 For Br analysis, a mass resolution of 21,000 was used with a 2000 μm Field Aperture giving

284 an analysed region of ~7 × 10 μm. Each analysis consisted of 10 measurement cycles with

285 ^{30}Si^{16}O$_3$ being measured for 2 s each cycle and ^{79}Br and ^{81}Br measured for 5 s each cycle. For

286 Br we used GSC-1G, GSE-1G, GSD-1G, BB1 and BB2 (figure S2) as our standard reference

287 materials (Marks et al. 2017; Kendrick 2012). The halogen concentrations of the unknown

288 glasses were then calculated as follows:

289

290
$$Br_{concentrations} = \frac{^{81}Br\,(cps) + ^{79}Br\,(cps)}{\left[^{30}SiO^{16}O_3 \dfrac{cps}{Si_{conc}\,(known)} \right]} * Relative\ Ion\ Yield$$

291   where the Relative Ion Yield is given by= (Ion Yield of Br/ Ion Yield Si) for an average of

292   multiple primary standards (table S2; figure S3) mounted in each sample block, and

293   Ion Yield Br = [^{79}Br (cps) + ^{81}Br (cps)]/known Br concentration (primary standard),

294   Ion Yield Si = ^{30}Si^{16}O$_3$ (cps)/known Si concentration (primary standard).

295   The Si content of the experiments was sometimes higher than the standards for Br (table S2),

296   however as Br ionises well, as shown by relatively stable signal intensities, matrix glass

297   effects are considered here to be minimal. This is supported by the secondary standard

298   comparison plot (figure S2) for the five secondary standards, each with a different major

299   element composition, showing a good match between measured and accepted values.

300   Typically, seven analyses were measured per sample. Mean concentrations and standard

301   deviations are given in table 3, and show good reproducibility. Along with the unknown

302   samples, MPI-DING secondary reference glasses were measured throughout the analysis

303   session to check for reproducibility, accuracy and drift (table S2). Limits of detection

304   (estimated based on the number of counts per time counted, see table S2) for Cl and F were

305   calculated on reference glasses StHs80 for F and Cl, and scapolite BB1 and GSE-1G for Br,

306   equating to 0.5 ppm, 1.3 ppm and 0.35 ppm for F, Cl and Br respectively.

307   We found that the halogen concentrations for the secondary reference materials varied

308   slightly between different mounts, potentially affected by the sample height, suggesting that

309   calibration should be conducted on the same mounts as the sample analysis if possible.

310

311   **RESULTS**

Petrological description of run products

313   The run products range in glass contents from 28-47 wt% for Kelud, and 82-94 wt% in the

314   Quizapu experiments (table 1). No new phases relative to the starting materials appeared

315   during the experiments, however in some of the lower-temperature experiments, more

316   evolved rims can be observed in backscattered images, compared to some more primitive

317   crystal cores (figure S1). This suggests that mineral rims grew in equilibrium with the melt as

318   intended by experimental design, without reacting with the more primitive mineral cores

319   (Pichavant et al., 2007). The experimental glass was microlite poor (figure S1), and contained

320   vapour vesicles, indicative of fluid-saturation, which was confirmed by puncturing and

321   heating the capsule post-experiment and determining relative mass loss. Repeat analyses of

322   major element and halogen concentrations (n=7-24) of experimental glass showed them to be

323   homogenous (fig. 2) within analytical uncertainty (table S3), suggesting that the time chosen

324   to reach chemical equilibrium was appropriate (table 1).

Halogen concentrations in matrix glass

326   Although Cl measured both by electron microprobe (EMPA) and SIMS (figure S4),

327   correlated fairly well, the concentrations of Cl were close to or below the limit of detection

328   for EMPA, as the instrument set-up was not optimised for Cl measurements. We therefore

329   report SIMS results in this paper, with their precision values <12%, and accuracy (<20% for

330   Br, and <2% for Cl & F values >100 ppm) supported by analysis of secondary reference

331   glasses (table S2).

332   The mean values, measured by SIMS, for the Kelud matrix glass composition (dacite) were:

333   F = 564 ppm (±56; 1 standard deviation of reproducibility), Cl = 1476 ppm (±14), and Br =

334   4.3 ppm (±0.4). For the Quizapu matrix glass composition (rhyolite): F = 661 ppm (±44), Cl

335   = 2192 ppm (±100), and Br = 6.1 ppm (±0.75) (table 2). Note that two bromine

336   measurements of 0.42 ppm (Quiz 3) and 0.54 ppm (Quiz 5) are close to the detection limit of

337   bromine of 0.35 ppm. Minor quantities of hydrous minerals (<1 % of halogen-bearing apatite

338   and <2% amphibole in the Quizapu experiments) may slightly alter the absolute halogen

339   contents in bulk starting material experiments.

340   Experimental matrix glass compositions range from andesitic to rhyolitic for Kelud (table 1;

341   figure 2), with the Quizapu experiments limited to rhyolitic glass compositions (table 3). The

342   range of compositions exhibited in the experimental glasses can be attributed to varying

343   amounts of melting and crystallisation resulting from the varying experimental run

344   temperatures, fluid contents and compositions (X_{H2O}). Thus, variable crystallinity may dilute

345   or enrich the halogen content in the glass for different experiments (table 1). Figure 2shows

346   SiO_2 versus Cl, F and Br glass concentrations for all experiments. For the Kelud starting

347   composition (Table 2), the experimental products with more evolved compositions contain

348   higher F, Cl and Br concentrations in the natural matrix glass. These positive correlations

349   with SiO_2 for fluorine ($R^2 = 0.68$), chlorine ($R^2 = 0.73$) and bromine ($R^2 = 0.55$) exist despite

350   changes in experimental pressure, temperature and volatile composition. For the Quizapu

351   starting composition (Table 2), this trend of increasing halogen concentrations at higher SiO_2

352   concentrations is apparent, despite the more limited range in compositions in the

353   experimental matrix glass, e.g., for fluorine $R^2=0.54$. For chlorine and bromine the

354   correlation only exists for the water saturated experiments ($X_{H2O} = 1$), with correlation

355   coefficients R^2 of 0.76, and 0.96 for Cl, and Br respectively. The mixed volatile experiments

356   from Quizapu (green open symbols, figure 2) mostly fall within the same range as the water

357   saturated experiments.

358   **Halogen fluid composition**

16

359   To work out the fluid composition required for calculating the fluid/melt partitioning, we

360   used a simple mass balance approach similar to Cadoux et al. (2018):

Mass (g) of halogen in fluid

$$= Mass\ of\ halogen\ in\ starting\ glass - Mass\ of\ halogen\ in\ final\ glass$$

361   Whereby,

362   Mass of halogen in starting powder = Concentration of halogen in starting powder (ppm)*10^{-}

363   ^{6} x Mass of starting powder (g).

364   The measured masses were converted into mass of glass, by correcting for the crystal fraction

365   in the starting material and the final glass as measured with SEM image analysis (table 1).

366   *Mass (g) of halogen in the final glass = Concentration of halogen in final glass (ppm)*10^{-6} x*

367   *Corrected mass of final glass (g)*

368   The corrected mass of the final glass is calculated from the initial mass of glass combined

369   with the mass of volatiles added to the capsule that dissolved within the melt. This correction

370   involves the respective gain and/or loss of water and CO_2, which partitioned from the volatile

371   phase in favour of the melt phase during the course of the experiment. These volatile contents

372   were modelled using a MELTS H_2O and CO_2 solubility model, requiring the pressure,

373   temperature, X_{H2O} and melt composition (Gualda and Ghiorso 2015). The modelled volatile

374   contents are comparable to other models (e.g., Papale et al., 2006).

375   *Fluid concentration of halogen (ppm)= mass (g) of halogen in fluid/ corrected final fluid*

376   *mass (g) x 10^{6}*

377   The uncorrected fluid mass was the measured weight of added volatiles to the capsule. The

378   mass difference between the final and initial glass was subtracted to give the corrected fluid

379   mass. At equilibrium during high P-T experiments there is a subtle impact of partial

380 dissolution of the aluminosilicate melt into the coexisting volatile phase (Burnham 1967). At

381 the relatively low pressures of these experiments, Burnham (1967) showed that only a small

382 amount of solute dissolved into the co-existing fluid (<2 wt%). A 2% correction was made to

383 the masses of the initial powder and volatile phase for all experiments.   The partition

384 coefficient for each halogen was calculated by dividing the halogen concentration of the fluid

385 by that of the melt.

386   Uncertainties were propagated using the minimum and maximum halogen

387 concentrations in the initial and experimental glasses, adjusting for crystal content calculation

388 errors (±5 wt%), weighing errors and calculated masses of H_2O and CO_2 (table 3). The

389 propagated errors are plotted in figures 4-8. Previous studies have shown that these

390 propagated errors often overestimate the absolute error and thus can be considered maximum

391 values (e.g., Alletti et al., 2014; Cadoux et al., 2018). Finally, Quizapu and Kelud both

392 contain trace amounts of apatite (<1 vol%) and Quizapu contains ~2 vol% hornblende

393 (Hildreth and Drake 1992 Ruprecht et al., 2012; Jeffery et al., 2014; Cassidy et al., 2016;

394 2019; First et al. 2021). Hydrous minerals may incorporate halogens into the mineral

395 structure, but the low abundance of hydrous minerals, coupled with knowledge of

396 mineral/melt partitioning values (e.g., Doherty et al., 2014; Iveson et al., 2017; Marks et al.,

397 2017) suggests that minor amounts of crystallisation or melting of apatite and/or hornblende

398 during the experiment would have a minimal effect on our $D^{fluid/melt}$ values. Given typical F

399 and   Cl contents in hornblende for Quizapu and arc magmas, this constitutes <10 ppm of

400 Cl, and <50 ppm of F being added to the melt if hornblende is completely dissolved.

401 **Fluid/melt halogen partitioning**

402 No additional halogen sources were added to the starting materials and given that measured

403 melt Cl contents are an order of magnitude below the modeled maximum Cl solubilities

404   (Figure 3) (Webster et al., 2015), none of these experiments reached hydrosaline brine

405   saturation, despite the addition of CO_2 in some experiments, which can lower the threshold

406   for brine-saturation (Joyce and Holloway, 1992). The run product glasses lie within the

407   experimentally constrained '200 MPa melt + aqueous vapour field' for rhyolitic melts in

408   equilibrium with a low-density volatile phase (Webster et al., 2015, figure 3).

409   For all experiments, the halogen fluid concentrations show broad positive correlations with

410   bulk fluid/melt partition coefficients consistent with other studies, and largely independent of

411   temperature, pressure and volatile contents (Figures 4 and 5). Fluid concentration

412   uncertainties were slightly higher for F and Br mass balance calculations, and these graphs

413   show more scatter than for Cl, which is a function of the larger range measured in glass

414   halogen contents for these experiments. The mixed volatile experiments ($X_{H2O} = 0.55$) fall on

415   the generally positive trend, as do the higher pressure (100 MPa) Kelud experiments. A clear

416   outlier to the generally positive correlations is Quiz 3 (850° C, $X_{H2O} = 1$, Table 3), which

417   yields higher than expected fluid/melt partitioning values relative to its fluid concentration

418   (e.g., Figure 4). This can be attributed to a higher actual fluid mass than calculated, which is

419   corroborated by the prominent H_2O resorption haloes around the bubbles in the SEM images

420   for Quiz 3 (figure S1). Consequently, this point was removed from the following dataset

421   presented.

422 **Partitioning and Ionic radius**

423 Bureau et al. (2000) suggested that $D^{fluid/melt}$ increases with ionic radius for halogens in albite

424 melt, although Cadoux et al., (2018) suggested further complexity to this relationship

425 depending on melt composition and volatile content and based on deductions from gas

426 geochemistry. The new experiments presented here are consistent with $D^{fluid/melt}$ increasing

427 with ionic radius (Figure 5), though with higher $D_F^{fluid/melt}$ values than Bureau et al., (2000).

428 On average, $D^{fluid/melt}$ for F (smallest ionic radius, D = 1.4 ± 0.51 (mean absolute error)) is

429 lower than Cl (D = 6.4 ± 0.9), which is in turn lower than Br (largest ionic radius; D = 16.5 ±

430 6.5). These values are within the range measured for halogens in other studies on similar melt

431 compositions (table S1). The average data can be fitted using an exponential function with a

432 R^2 of 0.95, but the best fitted data is the Quizapu dataset shown in green (figure 5; R^2= 0.99).

433 The less evolved Kelud experiments have a lower average bulk $D^{fluid/melt}$ than the more

434 evolved Quizapu experiments for chlorine and bromine, but yield higher values for fluorine.

435 This observation may not be significant given the range of partitioning values, however it is

436 consistent with the more evolved granitic melt value (76 wt% SiO_2 from Webster, (1990) for

437 $D_F^{fluid/melt}$ which is even lower.

438 **Halogen fluid/melt partitioning as a function of changing intrinsic variables**

439 To assess the effects of varying melt composition on halogen $D^{fluid/melt}$, we plot our

440 experimental data against the Larsen differentiation index

441 $(0.33 \times SiO_2 + K_2O) - (FeO + MgO + CaO)$ (Larsen, 1938) (Figs. 6A, B & C). This has been

442 shown to be a useful index for characterising evolving melt composition especially for Cl

443 (e.g., Webster et al., 2020). It accounts for elements known to control Cl solubility (e.g. Ca,

444 Mg and Fe; Webster et al., 2015), without using Na, which is prone to electron-beam

445 migration in hydrous glasses. The Quizapu data show a very limited compositional change,

446   yet a range in $D^{fluid/melt}$ (Figs. 6A, B & C). In contrast, the Kelud experimental glasses exhibit

447   a wide range in glass compositions (andesite to rhyolite) and form shallow negative trends

448   with respect to $D^{fluid/melt}$ with R^2 all above 0.72, with Cl particularly well correlated. In the

449   case of fluorine, this trend extends towards the more evolved Quizapu compositions (R^2=0.5)

450   (figure 6A). However, there is no significant trend with differentiation for Br and Cl when

451   Kelud and Quizapu datasets are combined. The melt differentiation trends in the Kelud

452   dataset occur despite superimposed differences in pressures, CO_2-H_2O mixtures, temperatures

453   and potential errors relating to the fluid calculation.

454   Kelud and Quizapu experiments show opposite trends as a function of temperature (figure

455   6D, E & F). While $D^{fluid/melt}$ in the Quizapu dacite series decreases with higher temperature,

456    $D^{fluid/melt}$ in Kelud increases with temperature. The temperature effect on $D^{fluid/melt}$ values is

457   most pronounced for the Quizapu dataset and for Br (R^2= 0.61), with F less temperature-

458   dependent. Due to the large uncertainties of some Quizapu experiments, variance-weighted

459   regression was applied to temperature correlation, providing higher revised R^2 correlations of

460   0.82, 0.87, and 0.81, for F, Cl and Br respectively.

461   All experiments were fluid saturated, but mixed volatile experiments with varying CO_2 and

462   H_2O ratios were run to assess their effect on fluid/melt partitioning of halogens (figure 6). In

463   both the Kelud and Quizapu dataset, the CO_2 bearing experiments (X_{H2O} = 0.55) lie along the

464   same trends as the X_{H2O} = 1 series, however the CO_2 bearing experiments generally show

465   lower $D^{fluid/melt}$ values (Figure 6). For the Kelud experiments, mean fluid/melt partition

466   coefficients for the X_{H2O} = 1 experiments are F= 2 ± 1.9 (1 s.d), Cl = 4.4 ± 3.8, and Br = 8.8 ±

467   6.6 (n=6). For the X_{H2O} = 0.55 experiments these are F= 0.8 ± 0.3, Cl= 0.4 ± 0.4 and Br= 2.3

468   ± 0.1 (n=2). For Quizapu, the X_{H2O} = 1 experiments had mean fluid/melt ratios of; F= 0.1 ±

469   0.1, Cl= 9.3 ± 3.4, and Br= 22.7 ± 13.7 (n=2); whilst the X_{H2O} = 0.55 experiments had

470    $D^{fluid/melt}$ values; F= 1.4 ± 1.3, Cl= 12.3 ± 2.9 and Br= 37.1 ± 22.8, showing higher $D^{fluid/melt}$

471   values.

472   Figure 7 highlights in detail how $D^{fluid/melt}$ covaries with various elements for the combined

473   Kelud and Quizapu experimental dataset. Pearson correlation values suggest that $D_{Cl}^{fluid/melt}$

474   and $D_{Br}^{fluid/melt}$ generally behave in a similar way (correlation coefficient = 0.88), with highest

475   negative correlations for Ti (also Na in the case for Cl) and positive correlations Al and K.

476   While $D_{F}^{fluid/melt}$ behaves markedly differently from $D_{Cl}^{fluid/melt}$ and $D_{Br}^{fluid/melt}$ (coefficient =

477   0.24 and 0.26) and negatively correlates best with Si, Na, K, with positive correlations for Fe,

478   Mg and Ca. The differences between the Kelud and Quizapu datasets can be seen in figures

479   S5 & S6.

480   **Halogen fluid/melt partitioning across different studies**

481   Values for $D_{Cl}^{fluid/melt}$ are all <20 (figure 6B and E), in line with other studies at similar melt

482   compositions and experimental conditions (e.g., Baker & Alletti, 2012; Webster et al., 1999;

483   Zajacz et al., 2012) (table S1). The majority of experiments show that Cl predominantly

484   partitions into the fluid phase over the melt phase, with the exception of two Kelud

485   experiments ($D_{Cl}^{fluid/melt}$ <1). Relative to Cl, absolute $D_{F}^{fluid/melt}$ values are lower (<6) with a

486   cluster around 1 for the most differentiated melts. Values for Br partitioning are the highest

487   among the halogens measured in this study, a trend observed by Bureau et al. (2000), with

488   most partition coefficients ranging between 2 and 36 (table S1). In contrast to Cl and F,

489   which partition into the melt under some conditions, our Br data show that it strongly

490   partitions into the fluid phase in all the experiments.

491   Figure 8 plots our experiments in the context of other data from the literature (see figure S7

492   for full breakdown of the different studies). We use the aluminosity index A/CNK (molar

493   Al/(Ca + Na + K), as Cl and F melt solubility are affected by increasing network-modifying

494   Na, K and Ca relative to Al (figure 7) (Webster 1992; Signorelli and Carroll, 2000; Webster

495   et al., 2015). The literature data plotted are from experiments thought to be in the brine-

496   undersaturated region for Cl, F, and therefore thought to represent Henrian partitioning. This

497   was estimated using the region of parameter space defined in previous studies (e.g., Cl <0.25

498   wt%, and F <4 wt%; cf., Baker & Alletti, 2012; Dolejš & Zajacz, 2018; Shinohara, 2009;

499   Webster et al., 2015; Zajacz et al., 2012). However, some CO_2 bearing experiments from the

500   literature may be in the brine field, as the presence of CO_2 lowers the threshold for brine

501   saturation (e.g., Joyce and Holloway 1993). Figure 8 broadly highlights that the fluid/melt

502   partition coefficients found in this study overlap with literature experiments at similar values

503   on the aluminosity index. The Quizapu dataset for instance, has similar values to those of

504   Alletti et al. (2009) and Botcharnikov et al. (2015), yet higher than others (Zajacz et al.,

505   2012). Kelud's experimental glass composition also overlapped with other studies (Hsu et al.,

506   2019; Webster et al., 2017; Webster & Holloway, 1990) and provides similar partitioning

507   values. The literature data for CO_2 mixed volatile experiments on figure 8 are plotted as open

508   circles and these generally occupy lower fluid/melt ratios for Cl (mean= 9.2, compared to

509   water saturated experiments (mean = 15), however their relative standard deviations both

510   exceed 100%. For CO_2-bearing F partitioning experiments, there is only this study and a few

511   data points from Webster et al. (2014) to compare (figure 8b), nevertheless the presence of

512   CO_2 did not significantly influence $D_F^{fluid/melt}$. The only Br mixed volatile data are from this

513   study and do not show significant differences with water-saturated experiments. Apart from

514   the mixed volatile experiments, the data compilation in Figure 8 broadly shows that lower

515   A/NCK values are associated with lower Br fluid/melt ratios (see also table S1). For F

516   however, the opposite is true, with higher $D_F^{fluid/melt}$ values at the lower A/CNK values. There

517   is no clear trend for $D_{Cl}^{fluid/melt}$, which speaks to the range of experimental conditions and the

518   complexity of these data as well as the clustering of experiments in certain areas of A/CNK

519   space (e.g., a sparsity of experiments at higher values).

<div align="center">

DISCUSSION

</div>

520

Halogen Partitioning and its influences

521

522   The concentration of Cl in the fluid phase has been established as one of the primary controls

523   on fluid melt partitioning (e.g., Webster, 1992), which is confirmed by this study for Cl and

524   also for F and Br (figure 4). The scatter in the data, i.e., for a constant halogen fluid

525   concentration, may be explained by the differing melt compositions and conditions (Dolejs &

526   Zajacz, 2018). The sections below will cover how our experimentally derived halogen

527   partitioning data are influenced by key variables such as ionic radius, melt composition, X_{H2O}

528   and temperature, in the context of previous studies. Whilst much of this has been studied for

529   Cl, there is complexity (e.g. Figure 8), and fewer data points exist for F and Br (figure 1).

Effect of ionic radius

530

531   Bureau et al. (2000) observed that for an albite melt composition, increasing fluid/melt

532   partitioning values from F, Cl, Br to I correlate with increasing ionic radii of the anion (figure

533   5). This relationship has also been shown for the fluid/melt partitioning behaviour of the

534   alkali metals Li, K, and Rb (e.g., Iveson et al., 2019). This result agrees with previous studies

535   which dictate that for the larger anions (Cl and Br) there is a greater mismatch with the ionic

536   radius of O, making them less likely to be incorporated in the aluminosilicate network

537   (Bureau et al., 2000). The iodine partitioning data of Bureau et al. (2000) (Figure 5), can be

538   used to extend the partitioning – ionic radius correlation from our Quizapu (rhyolite glass)

539   experiments (R^2=0.99), which is more similar in composition to Bureau et al. (2000) than the

540   Kelud dataset. We use this correlation to form a revised weighted regression equation for

541   rhyolitic melts based on our experiments as a function of ionic radius:

542      $D_{Halogen}^{fluid/melt} = e^{(5.46(\pm0.09) \text{ x } Å - 7.41(\pm0.12))}$, where Å is the ionic radius in Angstrom.

543   The gradient of the slope (and thus the preceding equation), will vary as a result of the

544   chemical composition, for instance mafic melts with higher $D_F^{fluid/melt}$ (Fig 6 & 8) will lead to

545   shallower gradients and vice versa (e.g., Bureau et al., 2000). The large variability in these

546   values means that the highest $D_F^{fluid/melt}$ values are sometimes higher than the lowest

547      $D_{Br}^{fluid/melt}$ values (Fig. 5), suggesting that other factors such as differences in halogen fluid

548   concentrations, melt compositions, pressure, temperature and X_{H2O} may account for the

549   variability in this trend.

Effect of melt composition

551   The two different starting compositions used in this study (whole rock basaltic andesite and

552   dacite, with dacitic and rhyolitic initial matrix glass compositions respectively) and variable

553   P-T conditions produced a range of different melt compositions, which allows us to explore

554   the role of composition on fluid/melt partitioning. Taking both datasets together, the highest

555      $D_{Cl}^{fluid/melt}$ and $D_{Br}^{fluid/melt}$ values are found in the most differentiated melts (Figure 6), yet the

556   least differentiated melts did not necessarily show the lowest fluid/melt partitioning. In

557   contrast, $D_F^{fluid/melt}$ shows the opposite trend across both datasets, with increasing

558   differentiation leading to lower average $D_F^{fluid/melt}$ values (Figure 6).

559   The notion of increased Cl in the fluid phase at more evolved compositions has been

560   observed in multiple studies (e.g., Webster and De Vivo, 2002) and also for Br (Cadoux et

561   al., 2018). This is likely related to the incompatible nature of the larger ions, Cl and Br in

562   melts during differentiation, lower charge densities of Cl and Br relative to F, coupled by the

563   higher degree of polymerisation, which makes the incorporation of larger anions into the melt

564   more difficult. More differentiated magmas have been predicted to have lower $D_F^{fluid/melt}$,

565   based on the ability of F to replace hydroxyl and oxygen ions in minerals, and substitute for

566 O on the vertices of aluminate or silicate tetrahedral, meaning that it preferentially favours

567 the melt relative to fluid phase as magma becomes more silicic during differentiation (Dolejš

568 & Baker, 2007; Webster, 1990). Our data help to confirm this inference (figure 7) by filling a

569 compositional gap in pre-existing experimental data, and demonstrating higher $D_F^{fluid/melt}$, i.e.,

570 more F partitioning into the fluid phase, in less evolved magmas.

571 Contrary to the overall observation of high $D_{Cl}^{fluid/melt}$ and $D_{Br}^{fluid/melt}$ for the most

572 differentiated magmas, within the Kelud dataset we find negative correlations with respect to

573 $D_{Cl}^{fluid/melt}$, and $D_{Br}^{fluid/melt}$ with differentiation (Figure 6), which exist despite removing the

574 concentration of halogens in the fluid as a factor. However, combining the Kelud and

575 Quizapu datasets shows no significant effect of differentiation (Figure 6), thus differentiation

576 alone may not be able to explain the distribution of $D_{Cl}^{fluid/melt}$ and $D_{Br}^{fluid/melt}$ values. The

577 compositional influence on partitioning may be more complex than mafic versus felsic, but

578 instead related to the availability of metal cations which form ligand complexes with F, Cl

579 and Br. For instance, the negative correlation between differentiation with $D_{Cl}^{fluid/melt}$ and

580 $D_{Br}^{fluid/melt}$ for the Kelud dataset, which encompasses a larger range of compositions than

581 Quizapu (Figure 6), is likely controlled by Na, K and Si complexes forming within these

582 experimental melts (figure S5, S6). Figure 7 combines both Quizapu and Kelud datasets and

583 highlights the potential halogen complexes forming in all the experimental melts, by elements

584 anti-correlated with $D^{fluid/melt}$ (e.g., K, Na, and Si for fluorine, Na, Ti for chlorine and Ti

585 bromine). The type of metal-ligand bonds that form (e.g. Na-Cl, K-Cl) can be related to both

586 the similarity in their orbital energy and the Lewis acidity or basicity of the cation and anion

587 pair.

588 The latter can be conceptualised following the bond valence model from Brown (2000),

589 which uses ion charge and coordination number to provide bond strength indicators in

590 valence units (v.u.) for individual ions, which correlates with electronegativity. For instance,

591 cations and anions with similar bond strengths (e.g., Na^+ – 0.16 v.u., and Cl^- - 0.13 v.u.) and

592 with the same number of atomic orbitals will be more likely to form strong associations,

593 relative to cations that have larger bond strength differences, e.g., Cl^- with Ca^{2+} (0.27 v.u.)

594 and less orbital overlap (e.g., K-Cl). These relationships are highlighted in the correlative plot

595 in Figure 7, showing the Na^+ is anticorrelated with $D_{Cl}^{fluid/melt}$, whereas Ca^{2+} and K^+ are not. It

596 is possible that some of the positive elemental correlations with $D^{fluid/melt}$ in Figure 7 may

597 indicate preferential complexes forming within the aqueous fluid (e.g., KCl, CaF_2, KBr). The

598 negative correlations between Ti and $D_{Cl}^{fluid/melt}$ and $D_{Br}^{fluid/melt}$ (figure 7) are not found in

599 either Kelud or Quizapu datasets separately, unlike other elemental correlations (Figures S5

600 & S6) and are therefore likely an artefact of bringing the two datasets together with

601 inherently different Ti contents (Figure 7). The strong association between Si and F in our

602 experiments (figure 7) is explained by high silicon-fluorine bond strength, resulting from

603 their high charge densities (e.g., Dolejs and Baker, 2006; Dalou and Mysen, 2015). Some

604 studies suggest that halide complexes with Mg, Ca, and Al are also important (Webster et al.,

605 2015), but this was not observed in our study. The strong elemental associations in the melt

606 observed here (e.g., NaCl, SiF_4) are more consistent with in situ spectroscopic measurements

607 (Dalou et al., 2015; Louvel et al. 2020).

608 The inclusion of other volatile species such as sulfur, may also affect $D_{Cl}^{fluid/melt}$ by altering

609 the nature of the complexes that form (Webster et al. 2009; Beermann, 2010). This effect

610 seems to be dependent on the oxidation state, with $D_{Cl}^{fluid/melt}$ increasing with the addition of

611 oxidised sulfur to the melts (Botcharnikov et al. 2004; Webster et al. 2003; Beermann 2010),

612 due to the enhanced stabilisation of Na, K and Ca in S-bearing saline fluids. However, this

613 effect is minimal at lower oxygen fugacities of NNO-0.5 (Zajacz et al. 2012). Sulfur

614 concentrations were not measured here, but are likely be higher in the Quizapu samples,

615 which evidenced by the presence of sulfide blebs visible under SEM (Ruprecht et al., 2012),

616   compared to the Kelud samples where they were absent, and this may explain the different

617   halide complexes formed in the melt (Na, K and Si for Kelud figure S5 & compared to Fe for

618   Quizapu, figure S6). The reader is referred to Webster et al. (2020) for further discussion of

619   the effect of oxidised vs. non-oxidised S on Cl solubility behaviour.

620   The alumina-saturation index (molar $Al_2O_3/(Na_2O+K_2O+CaO)$) has been shown to influence

621   halogen fluid/melt and crystal/melt partitioning behaviour (e.g., Olin and Wolff 2012; Iveson

622   et al. 2019), potentially accounting for some of the influence from these metal-ligand

623   complexes (Fig. 8). Some broad trends of higher $D_{Br}^{fluid/melt}$ and lower $D_F^{fluid/melt}$ with

624   increasing aluminosity exist, which can be attributed to presence or absence of Na, K

625   complexes. However, there is significant scatter, partly due to the combination of different P-

626   T experimental conditions, and partly because more elements than just Al, Na, K and Ca are

627   involved in the formation of melt halide complexes.

628   **Effect of temperature**

629   There are relatively few experiments that attempt to assess the influence of temperature on

630   halogen partitioning. Most data suggest that temperature has a minor effect on Cl, relative to

631   the much stronger controls of melt and fluid composition (Chevychelov et al., 2008; Stelling

632   et al., 2008; Iveson et al., 2019). Bromine, however, may show stronger temperature

633   dependence (Cadoux et al., 2018). Correlations between Cl, F and Br fluid/melt partitioning

634   and temperature are clearly evident in our experiments (Figure 6), however for the Quizapu

635   dataset this correlation is negative, with decreasing $D^{fluid/melt}$ values with increasing

636   temperature, while the Kelud dataset shows the opposite trend. Because the temperature (and

637   pressure) of the experiment can also affect its melt composition through the crystallisation or

638   melting of mineral phases, it can be difficult to disentangle these two factors, especially since

639   melt composition has a dominant role in controlling fluid/melt partitioning. Certainly for the

640   Kelud experiments the change in the melt composition is large (58% - 73 wt% SiO_2; Figure

641   2), suggesting that the fluid/melt partitioning is most likely dominated by the change in melt

642   composition, overprinting any temperature effect (Figure 6). However, for the Quizapu

643   experiments there is a relatively smaller compositional change in the melt chemistry (69 - 74

644   wt% SiO_2; Figure 6). Therefore, the variation in experimental temperature (800 °C - 900 °C)

645   likely explains the negative correlation of $D^{fluid/melt}$ observed for the Quizapu experiments.

646   This concurs with the thermodynamic formulation from Thomas and Wood (2020) for

647   anhydrous basalts, which also shows that Cl solubility in melt should increase with increasing

648   temperature. This effect has been observed previously in experiments on Br partitioning,

649   which show increasing $D_{Br}^{fluid/melt}$ with decreasing temperatures (900-1200 °C (Cadoux et al.,

650   2018). The larger effect of temperature on $D_{Br}^{fluid/melt}$ compared to Cl (and especially F) may

651   be related to the relatively weaker metal-ligand bonds formed by Br in the melt, due to its

652   lower electronegativity and charge density, relative to Cl and F. The smaller ionic size of F

653   leads to larger lattice energies of fluorides and therefore higher temperature stability of F

654   complexes, which may explain the smaller temperature effect on $D_F^{fluid/melt}$.

655   **Effect of CO_2**

656   Five H_2O+CO_2-bearing experiments ($X_{H2O} = 0.55$) were conducted in this study and are

657   compared with fluid/melt partitioning values for the same composition, pressure and

658   temperature conditions. The $X_{H2O} = 0.55$ experiments follow similar compositional trends to

659   those defined for $X_{H2O} = 1$, suggesting that CO_2 did not have a strong influence on this trend

660   (Figure 6). In the Kelud dataset the $X_{H2O} = 0.55$ experiments show generally lower $D_{Cl}^{fluid/melt}$,

661   however these were also more differentiated and so the effect of melt composition may also

662   be a factor here (Fig. 6). Other studies suggest that the effect of CO_2 on $D_{Cl}^{fluid/melt}$

663   partitioning is variable, studies of andesitic, phonolitic and trachytic melts show that CO_2 in

664   the fluid has little influence on $D_{Cl}^{fluid/melt}$ (Botcharnikov et al. 2006; Webster et al. 2014),

665   whilst Alletti et al. (2009) observed decreasing values of $D_{Cl}^{fluid/melt}$ with increasing CO_2 in

666   fluids coexisting with trachybasaltic melt at 25–100 MPa. Hsu et al. (2019) assessed the role

667   of CO_2 systematically and found that CO_2 lowers $D_{Cl}^{fluid/melt}$. Following the empirical

668   regression of Hsu et al. (2019) based on granitic melts, we found that this equation could not

669   replicate the Cl partitioning values from our CO_2-H_2O experiments, although this seems to be

670   calibrated for slightly higher pressures than the run conditions of our experiments. Our

671   compilation (Figure 8) suggests that average $D_{Cl}^{fluid/melt}$'s for H_2O+CO_2 bearing experiments

672   are lower than the pure H_2O experiments, but this is not outside the variation of their ranges.

673   There is a limited dataset of CO_2-bearing experiments to assess F and Br fluid/melt

674   partitioning (Figure 8); these data suggest that CO_2 addition has only a minor effect on

675    $D_F^{fluid/melt}$ and $D_{Br}^{fluid/melt}$ when compared with other effects such as fluid and melt

676   composition, but this effect may differ for higher fluid salinity than used in this study.

677   **IMPLICATIONS**

678   This study provides key information about halogen behaviour in intermediate to silicic melts,

679   compositions typical of those produced in subduction zone magmas, which have received far

680   less study to date (Figure 1), but commonly result in hazardous explosive eruptions and the

681   generation of ores. Data across a wide range of compositions are required to build rigorous

682   models of halogen behaviour during volcanic processes. Using the approach outlined here of

683   not doping experiments with halogens, but analysing low concentrations with SIMS, opens

684   up the potential for the measurement of halogens in previously conducted phase equilibria

685   experiments. Our analysis supports the notion that melt composition has a strong control on

686   Cl, F and Br fluid/melt partitioning (e.g. Webster et al., 2018). Simple differentiation does not

687   control the variation of partitioning values for Cl and Br partitioning (Figure 6). Instead,

688   particular elements (e.g., K, Al, Na) with an affinity to make complexes with Cl and Br in the

689   melt, can explain 40 to 60 % of the variation in Br and Cl fluid/melt partition coefficients

690   (Figure 7). In contrast, F seems to favour the melt over the fluid with increasing

691   differentiation, with >70% of the variation in $D_F^{fluid/melt}$ explained by Si concentration alone

692   (Figure 2, Figure 7). This observation may be applied to the interpretation of magmatic

693   processes in melt inclusions and hydrous minerals (retrospectively), or volcanic gas

694   monitoring (in real time). For instance, measurements of volcanic gas species are used to

695   interpret changing depth of magma, since H_2O, S and CO_2 solubilities are particularly

696   sensitive to pressure and oxidation state (e.g., de Moor et al., 2016). However if S, H_2O and

697   CO_2 fluxes, and associated ratios remain constant, but halogen ratios such as (Cl+Br)/F ratios

698   increase over time, this could point to differentiation, or even temperature changes of an

699   underlying stationary magma reservoir (e.g., Aiuppa et al. 2002, 2007; Edmonds et al. 2003,

700   2009; Allard et al. 2005; Burton et al. 2007; Balcone-Boissard et al. 2010; Bobrowski and

701   Giuffrida 2012; Christopher et al. 2015). The strong relationship of $D_F^{fluid/melt}$ with melt

702   composition, which decreases both with differentiation (Figure 6) and degree of aluminosity

703   (Figure 8), might also explain the higher extent of F degassing in basaltic and alkaline lava

704   lakes relative to silicic stratovolcanoes; the former may be accentuated by gas exsolution in

705   equilibrium at shallow pressures, <10 MPa (e.g., Edmonds et al. 2009; Oppenheimer et al.

706   2011). Individual magmatic volatile species are variably affected by different magmatic

707   processes and conditions, such that by measuring a larger set of volatile species in melt

708   inclusions, such as CO_2, H_2O, S along with F, Cl, and Br, one may be able to disentangle

709   these magmatic conditions and processes prior to eruptions. For instance, trends towards

710   higher (Cl+Br)/F melt ratios may indicate mafic injection due to the compositional effects,

711   whereas trends to lower (Cl+Br)/F ratios, with increasing H_2O, and relatively constant S, may

712   point to differentiation of a stationary magma reservoir leading to second boiling. By

713   providing more fluid/melt partitioning data for a range of subduction zone magma

714   compositions, these will also aid the calculation (e.g., via the melt inclusion petrological

715 method) of Cl, F and Br fluxes into the atmosphere for historical eruptions sourced from

716 intermediate and silicic magmas, which have the potential for significant stratospheric ozone

717 destruction (e.g. Kutterolf et al. 2013; Cadoux et al. 2015; Vidal et al., 2016; Cadoux et al.,

718 2015).

719

Acknowledgements

728

REFERENCES

730 Aiuppa, A., Federico, C., Paonita, A., Pecoraino, G., and Valenza, M. (2002) S, Cl and F

731 degassing as an indicator of volcanic dynamics: The 2001 eruption of Mount Etna.

732 Geophysical Research Letters, 29, 1–4.

733 Aiuppa, A., Federico, C., Franco, A., Giudice, G., Gurrieri, S., Inguaggiato, S., Liuzzo, M.,

734 McGonigle, A.J.S., and Valenza, M. (2005) Emission of bromine and iodine from

735 Mount Etna volcano. Geochemistry, Geophysics, Geosystems, 6, 1–8.

736 Aiuppa, A., Moretti, R., Federico, C., Giudice, G., Gurrieri, S., Liuzzo, M., Papale, P.,

737 Shinohara, H., and Valenza, M. (2007) Forecasting Etna eruptions by real-time

738   observation of volcanic gas composition. Geology, 35, 1115–1118.

739   Aiuppa, A., Baker, D.R., and Webster, J.D. (2009) Halogens in volcanic systems. Chemical

740   Geology, 263, 1–18.

741   Allard, P., Burton, M., and Mur, F. (2005) Spectroscopic evidence for a lava fountain driven

742   by previously accumulated magmatic gas. Nature, 433, 407–410.

743   Alletti, M., Baker, D.R., Scaillet, B., Aiuppa, A., Moretti, R., and Ottolini, L. (2009) Chlorine

744   partitioning between a basaltic melt and H_2O-CO_2 fluids at Mount Etna. Chemical

745   Geology, 263, 37–50.

746   Alletti, M., Burgisser, A., Scaillet, B., and Oppenheimer, C. (2014) Chloride partitioning and

747   solubility in hydrous phonolites from Erebus volcano: A contribution towards a multi-

748   component degassing model. GeoResJ, 3–4, 27–45.

749   Baker, D.R., and Alletti, M. (2012) Fluid saturation and volatile partitioning between melts

750   and hydrous fluids in crustal magmatic systems: The contribution of experimental

751   measurements and solubility models. Earth-Science Reviews, 114, 298–324.

752   Balcone-Boissard, H., Villemant, B., and Boudon, G. (2010) Behavior of halogens during the

753   degassing of felsic magmas. Geochemistry, Geophysics, Geosystems, 11.

754   Beermann, O., Botcharnikov, R.E., and Nowak, M. (2015) Partitioning of sulfur and chlorine

755   between aqueous fluid and basaltic melt at 1050°C, 100 and 200 MPa. Chemical

756   Geology, 418, 132–157.

757   Bell, A.S., and Simon, A. (2011) Experimental evidence for the alteration of the $Fe^{3+}/\Sigma Fe$ of

758   silicate melt caused by the degassing of chlorine-bearing aqueous volatiles. Geology, 39,

759   499–502.

760   Bobrowski, N., and Giuffrida, G. (2012) Bromine monoxide/sulphur dioxide ratios in relation

761   to volcanological observations at Mt. Etna 2006-2009. Solid Earth, 3, 433–445.

762 Bodnar, R.J., Lecumberri-Sanchez, P., Moncada, D., and Steele-MacInnis, M. (2013) Fluid

763   Inclusions in Hydrothermal Ore Deposits. In Treatise on Geochemistry: Second Edition.

764 Borodulin, G.P., Chevychelov, V.Y., and Zaraysky, G.P. (2009) Experimental study of

765   partitioning of tantalum, niobium, manganese, and fluorine between aqueous fluoride

766   fluid and granitic and alkaline melts. Doklady Earth Sciences, 427, 868–873.

767 Botcharnikov, R.E., Behrens, H., and Holtz, F. (2006) Solubility and speciation of C-O-H

768   fluids in andesitic melt at T = 1100-1300 °C and P = 200 and 500 MPa. Chemical

769   Geology, 229, 125–143.

770 Botcharnikov, R.E., Holtz, F., and Behrens, H. (2015) Solubility and fluid-melt partitioning

771   of H2O and Cl in andesitic magmas as a function of pressure between 50 and 500 MPa.

772   Chemical Geology, 418, 117–131.

773 Brown, I.D. (2000) The Bond Valence Model as a Tool for Teaching Inorganic Chemistry:

774   The Ionic Model Revisited. Journal of Chemical Education, 77, 1070–1075.

775 Bureau, H., and Métrich, N. (2003) An experimental study of bromine behaviour in water-

776   saturated silicic melts. Geochimica et Cosmochimica Acta, 67, 1689–1697.

777 Bureau, H., Keppler, H., and Métrich, N. (2000) Volcanic degassing of bromine and iodine:

778   Experimental fluid/melt partitioning data and applications to stratospheric chemistry.

779   Earth and Planetary Science Letters, 183, 51–60.

780 Burnham (1967) Hydrothermal fluids at the magmatic stage. In Geochemistry of

781   Hydrothermal Ore Deposits pp. 34–76. Holt, Rinehart, and Winston, New York.

782 Burton, M., Allard, P., Mure, F., and La Spina, A. (2007) Magmatic gas composition reveals

783   the source depth of slug-driven strombolian explosive activity. Science.

784   Cadoux, A., Scaillet, B., Bekki, S., Oppenheimer, C., and Druitt, T.H. (2015) Stratospheric

785   Ozone destruction by the Bronze-Age Minoan eruption (Santorini Volcano, Greece).

786   Scientific Reports, 5, 1–12.

787   Cadoux, A., Iacono-Marziano, G., Scaillet, B., Aiuppa, A., Mather, T.A., Pyle, D.M.,

788   Deloule, E., Gennaro, E., and Paonita, A. (2018) The role of melt composition on

789   aqueous fluid vs. silicate melt partitioning of bromine in magmas. Earth and Planetary

790   Science Letters, 498, 450–463.

791   Cassidy, M., Castro, J.M., Helo, C., Troll, V.R., Deegan, F.M., Muir, D., Neave, D.A., and

792   Mueller, S.P. (2016) Volatile dilution during magma injections and implications for

793   volcano explosivity. Geology, 44, 1027–1030.

794   Cassidy, M., Ebmeier, S.K., Helo, C., Watt, S.F.L., Caudron, C., Odell, A., Spaans, K.,

795   Kristianto, P., Triastuty, H., Gunawan, H., and others (2019a) Explosive Eruptions With

796   Little Warning: Experimental Petrology and Volcano Monitoring Observations From the

797   2014 Eruption of Kelud, Indonesia. Geochemistry, Geophysics, Geosystems, 1–30.

798   Cassidy, M., Ebmeier, S.K., Helo, C., Watt, S.F.L., Caudron, C., Odell, A., Spaans, K.,

799   Kristianto, P., Triastuty, H., Gunawan, H., and others (2019b) Explosive Eruptions With

800   Little Warning: Experimental Petrology and Volcano Monitoring Observations From the

801   2014 Eruption of Kelud, Indonesia. Geochemistry, Geophysics, Geosystems, 20.

802   Chevychelov, V.Y. (2019) Partitioning of Volatile Components (Cl, F, and CO_2) in Water-

803   Saturated Fluid–Magma Systems of Various Composition. Petrology, 27, 585–605.

804   Chevychelov, V.Y., Bocharnikov, R.E., and Holtz, F. (2008) Experimental study of chlorine

805   and fluorine partitioning between fluid and subalkaline basaltic melt. Doklady Earth

806   Sciences, 422, 1089–1092.

807   Christopher, T.E., Blundy, J., Cashman, K., Cole, P., Edmonds, M., Smith, P.J., Sparks,

808   R.S.J., and Stinton, A. (2015) Crustal-scale degassing due to magma system

809   destabilization and magma-gas decoupling at Soufrière Hills Volcano, Montserrat.

810   Geochemistry, Geophysics, Geosystems, 16, 2797–2811.

811   Cochain, B., Sanloup, C., de Grouchy, C., Crépisson, C., Bureau, H., Leroy, C., Kantor, I.,

812   and Irifune, T. (2015) Bromine speciation in hydrous silicate melts at high pressure.

813   Chemical Geology.

814   Dalou, C., and Mysen, B.O. (2015) The effect of H_2O on F and Cl solubility and solution

815   mechanisms of in aluminosilicate melts at high pressure and high temperature. American

816   Mineralogist.

817   Dalou, C., Mysen, B.O., and Foustoukos, D. (2015) In-situ measurements of fluorine and

818   chlorine speciation and partitioning between melts and aqueous fluids in the Na_2O-

819   Al_2O_3-SiO_2-H_2O system. American Mineralogist, 100, 47–58.

820   Doherty, A.L., Webster, J.D., Goldoff, B.A., and Piccoli, P.M. (2014) Partitioning behavior

821   of chlorine and fluorine in felsic melt-fluid(s)-apatite systems at 50MPa and 850-950 °C.

822   Chemical Geology, 384, 94–109.

823   Dolejš, D., and Baker, D.R. (2007) Liquidus equilibria in the system K_2O-Na_2O-Al_2O_3-SiO_2-

824   F_2O-1-H_2O to 100 MPa: II. Differentiation paths of fluorosilicic magmas in hydrous

825   systems. Journal of Petrology.

826   Dolejš, D., and Zajacz, Z. (2018) Halogens in Silicic Magmas and Their Hydrothermal

827   Systems. The Role of Halogens in Terrestrial and Extraterrestrial Geochemical

828   Processes: Surface, Crust, and Mantle

829   Donovan, A., Tsanev, V., Oppenheimer, C., and Edmonds, M. (2014) Reactive halogens

830   (BrO and OClO) detected in the plume of Soufrière Hills Volcano during an eruption

831   hiatus. Geochemistry, Geophysics, Geosystems.

832 Edmonds, M., Herd, R.A., Galle, B., and Oppenheimer, C.M. (2003) Automated, high time-

833   resolution measurements of SO_2 flux at Soufriere Hills Volcano, Montserrat. Bulletin of

834   Volcanology, 65, 578–586.

835 Edmonds, M., Gerlach, T.M., and Herd, R.A. (2009) Halogen degassing during ascent and

836   eruption of water-poor basaltic magma. Chemical Geology, 263, 122–130.

837 Erdmann, S., Martel, C., Pichavant, M., Bourdier, J.L., Champallier, R., Komorowski, J.C.,

838   and Cholik, N. (2016) Constraints from phase equilibrium experiments on pre-eruptive

839   storage conditions in mixed magma systems: A case study on crystal-rich basaltic

840   andesites from Mount Merapi, Indonesia. Journal of Petrology, 57, 535–560.

841 First, E.C., Hammer, J.E., Ruprecht, P., and Rutherford, M. (2021) Experimental constraints

842   on dacite magma storage beneath Volcán Quizapu, Chile. Journal of Petrology.

843 Gualda, G.A.R., and Ghiorso, M.S. (2015) MELTS-Excel: A Microsoft Excel-based MELTS

844   interface for research and teaching of magma properties and evolution. Geochemistry,

845   Geophysics, Geosystems, 16, 315–324.

846 Gutmann, A., Bobrowski, N., Roberts, T.J., Rüdiger, J., and Hoffmann, T. (2018) Advances

847   in bromine speciation in volcanic plumes. Frontiers in Earth Science, 6, 1–24.

848 Hammer, J.E. (2008) Experimental studies of the kinetics and energetics of magma

849   crystallization. Reviews in Mineralogy and Geochemistry.

850 Harlov, D.E., and Aranovich, L. (2018) The Role of Halogens in Terrestrial and

851   Extraterrestrial Geochemical Processes: Surface, Crust, and Mantle.

852   Hildreth, W., and Drake, R.E. (1992) Volcán Quizapu, Chilean Andes. Bulletin of

853   Volcanology, 54, 93–125.

854   Hsu, Y.J., Zajacz, Z., Ulmer, P., and Heinrich, C.A. (2019) Chlorine partitioning between

855   granitic melt and H_2O-CO_2-NaCl fluids in the Earth's upper crust and implications for

856   magmatic-hydrothermal ore genesis. Geochimica et Cosmochimica Acta, 261, 171–190.

857   Iveson, A.A., Webster, J.D., Rowe, M.C., and Neill, O.K. (2017) Major element and halogen

858   (F, Cl) mineral-melt-fluid partitioning in hydrous rhyodacitic melts at shallow crustal

859   conditions. Journal of Petrology, 58, 2465–2492.

860   ——— (2019) Fluid-melt trace-element partitioning behaviour between evolved melts and

861   aqueous fluids: Experimental constraints on the magmatic-hydrothermal transport of

862   metals. Chemical Geology, 516, 18–41.

863   Jeffery, A.J., Gertisser, R., Troll, V.R., Jolis, E.M., Dahren, B., Harris, C., Tindle, A.G.,

864   Preece, K., O'Driscoll, B., Humaida, H., and others (2013) The pre-eruptive magma

865   plumbing system of the 2007-2008 dome-forming eruption of Kelut volcano, East Java,

866   Indonesia. Contributions to Mineralogy and Petrology, 166, 275–308.

867   Jochum, K.P., Stoll, B., Herwig, K., Willbold, M., Hofmiann, A.W., Amini, M., Aarburg, S.,

868   Abouchami, W., Hellebrand, E., Mocek, B., and others (2006) MPI-DING reference

869   glasses for in situ microanalysis: New reference values for element concentrations and

870   isotope ratios. Geochemistry, Geophysics, Geosystems, 7.

871   Joyce, D.B., and Holloway, J.R. (1993) An experimental determination of the thermodynamic

872   properties of H2O-CO2-NaCl fluids at high pressures and temperatures. Geochimica et

873   Cosmochimica Acta, 57, 733–746.

874   Kendrick, M.A. (2012) High precision Cl, Br and I determinations in mineral standards using

875   the noble gas method. Chemical Geology, 292–293, 116–126.

876 Kutterolf, S., Hansteen, T.H., Appel, K., Freundt, A., Krüger, K., Pérez, W., and Wehrmann,

877   H. (2013) Combined bromine and chlorine release from large explosive volcanic

878   eruptions: A threat to stratospheric ozone? Geology, 41, 707–710.

879 Louvel, M., Cadoux, A., Brooker, R.A., Proux, O., and Hazemann, J.L. (2020) New insights

880   on Br speciation in volcanic glasses and structural controls on halogen degassing.

881   American Mineralogist, 105, 795–80

882 Lowenstern, J.B. (1994) Chlorine, fluid immiscibility, and degassing in peralkaline magmas

883   from Pantelleria, Italy. American Mineralogist, 79, 353–369.

884 Marks, M.A.W., Wenzel, T., Whitehouse, M.J., Loose, M., Zack, T., Barth, M., Worgard, L.,

885   Krasz, V., Eby, G.N., Stosnach, H., and others (2012) The volatile inventory (F, Cl, Br,

886   S, C) of magmatic apatite: An integrated analytical approach. Chemical Geology, 291,

887   241–255.

888 Marks, M.A.W., Kendrick, M.A., Eby, G.N., Zack, T., and Wenzel, T. (2017) The F, Cl, Br

889   and I Contents of Reference Glasses BHVO-2G, BIR-1G, BCR-2G, GSD-1G, GSE-1G,

890   NIST SRM 610 and NIST SRM 612. Geostandards and Geoanalytical Research, 41,

891   107–122.

892 Moor, J.M., Aiuppa, A., Avard, G., Wehrmann, H., Dunbar, N., Muller, C., Tamburello, G.,

893   Giudice, G., Liuzzo, M., Moretti, R., and others (2016) Turmoil at Turrialba Volcano

894   (Costa Rica): Degassing and eruptive processes inferred from high-frequency gas

895   monitoring. Journal of Geophysical Research: Solid Earth, 1–15.

896 Olin, P.H., and Wolff, J.A. (2012) Partitioning of rare earth and high field strength elements

897   between titanite and phonolitic liquid. Lithos.

898 Oppenheimer, C., Moretti, R., Kyle, P.R., Eschenbacher, A., Lowenstern, J.B., Hervig, R.L.,

899   and Dunbar, N.W. (2011) Mantle to surface degassing of alkalic magmas at Erebus

900   volcano, Antarctica. Earth and Planetary Science Letters.

901 Papale, P., Moretti, R., and Barbato, D. (2006) The compositional dependence of the

902   saturation surface of $H_2O + CO_2$ fluids in silicate melts. Chemical Geology, 229, 78–95.

903 Pichavant, M., Costa, F., Burgisser, A., Scaillet, B., Martel, C., and Poussineau, S. (2007)

904   Equilibration scales in silicic to intermediate magmas - Implications for experimental

905   studies. Journal of Petrology, 48, 1955–1972.

906 Pyle, D.M., and Mather, T.A. (2009) Halogens in igneous processes and their fluxes to the

907   atmosphere and oceans from volcanic activity: A review. Chemical Geology, 263, 110–

908   121.

909 Ruprecht, P., and Bachmann, O. (2010) Pre-eruptive reheating during magma mixing at

910   Quizapu volcano and the implications for the explosiveness of silicic arc volcanoes.

911   Geology, 38, 919–922.

912 Ruprecht, P., Bergantz, G.W., Cooper, K.M., and Hildreth, W. (2012) The crustal magma

913   storage system of volcán Quizapu, Chile, and the effects of magma mixing on magma

914   diversity. Journal of Petrology, 53, 801–840.

915 Shinohara, H. (2009) A missing link between volcanic degassing and experimental studies on

916   chloride partitioning. Chemical Geology, 263, 51–59.

917 Sigurdsson, N.& (1981) NielsenQuantitative methods for electron microprobe analysis of

918   sodium in natural and synthetic glasses American Mineralogist2004.pdf.

919 Stelling, J., Botcharnikov, R.E., Beermann, O., and Nowak, M. (2008) Solubility of H_2O- and

920   chlorine-bearing fluids in basaltic melt of Mount Etna at T = 1050-1250 °C and P =

921   200 MPa. Chemical Geology, 256, 101–109.

922   Tattitch, B., Chelle-Michou, C., Blundy, J., and Loucks, R.R. (2021) Chemical feedbacks

923   during magma degassing control chlorine partitioning and metal extraction in volcanic

924   arcs. Nature Communications, 12.

925

926   Teiber, H., Marks, M.A.W., Wenzel, T., Siebel, W., Altherr, R., and Markl, G. (2014) The

927   distribution of halogens (F, Cl, Br) in granitoid rocks. Chemical Geology, 374–375, 92–

928   109.

929   Thomas, R.W., and Wood, B.J. (2020) The chemical behaviour of chlorine in silicate melts.

930   Geochimica et Cosmochimica Acta.

931   Vidal, C.M., Métrich, N., Komorowski, J.-C., Pratomo, I., Michel, A., Kartadinata, N.,

932   Robert, V., and Lavigne, F. (2016) The 1257 Samalas eruption (Lombok, Indonesia): the

933   single greatest stratospheric gas release of the Common Era. Scientific Reports, 6,

934   34868.

935   Webster, J.D. (1990) Partitioning of F between H_2O and CO_2 fluids and topaz rhyolite melt -

936   Implications for mineralizing magmatic-hydrothermal fluids in F-rich granitic systems.

937   Contributions to Mineralogy and Petrology, 104, 424–438.

938   ——— (1992) Water solubility and chlorine partitioning in Cl-rich granitic systems: Effects

939   of melt composition at 2 kbar and 800°C. Geochimica et Cosmochimica Acta.

940   ——— (1997) Exsolution of magmatic volatile phases from Cl-enriched mineralizing

941   granitic magmas and implications for ore metal transport. Geochimica et Cosmochimica

942   Acta, 61, 1017–1029.

943   Webster, J.D., and De Vivo, B. (2002) Experimental and modeled solubilities of chlorine in

944   aluminosilicate melts, consequences of magma evolution, and implications for

945   exsolution of hydrous chloride melt at Mt. Somma-Vesuvius. American Mineralogist,

946   87, 1046–1061.

947   Webster, J.D., and Holloway, J.R. (1990) and Highly Evolved Granitic Magmas.

948   Webster, J.D., Kinzler, R.J., and Mathez, E.A. (1999) Chloride and water solubility in basalt

949   and andesite melts and implications for magmatic degassing. Geochimica et

950   Cosmochimica Acta, 63, 729–738.

951   Webster, J.D., Goldoff, B., Sintoni, M.F., Shimizu, N., and De Vivo, B. (2014) C-O-H-Cl-S-

952   F volatile solubilities, partitioning, and mixing in phonolitic-trachytic melts and

953   aqueous-carbonic vapor ± saline liquid at 200MPa. Journal of Petrology, 55, 2217–2248.

954   Webster, J.D., Vetere, F., Botcharnikov, R.E., Goldoff, B., McBirney, A., and Doherty, A.L.

955   (2015) Experimental and modeled chlorine solubilities in aluminosilicate melts at 1 to

956   7000 bars and 700 to 1250 °c: Applications to magmas of Augustine Volcano, Alaska.

957   American Mineralogist, 100, 522–535.

958   Webster, J.D., Goldoff, B.A., Flesch, R.N., Nadeau, P.A., and Silbert, Z.W. (2017) Hydroxyl,

959   Cl, and F partitioning between high-silica rhyolitic melts-apatite-fluid(s) at 50-200 MPa

960   and 700-1000 °c. American Mineralogist, 102, 61–74.

961   Webster, J.D., Baker, D.R., and Aiuppa, A. (2018) Halogens in Mafic and Intermediate-Silica

962   Content Magmas. In The Role of Halogens in Terrestrial and Extraterrestrial

963   Geochemical Processes: Surface, Crust, and Mantle

964   Webster, J.D., Iveson, A.A., Rowe, M.C., and Webster, P.M. (2020) Chlorine and felsic

965   magma evolution: Modeling the behavior of an under-appreciated volatile component.

966   Geochimica et Cosmochimica Acta, 271, 248–288.

967   Zajacz, Z., Candela, P.A., Piccoli, P.M., and Sanchez-Valle, C. (2012) The partitioning of

968   sulfur and chlorine between andesite melts and magmatic volatiles and the exchange

969   coefficients of major cations. Geochimica et Cosmochimica Acta, 89, 81–101.

970

Figure Captions:

971

972   Figure 1. Total alkali silica plot for all the previous brine undersaturated experiments, along

973   with their corresponding pressures (MPa), for chlorine, fluorine and bromine. The grey

974   symbols represent the compositional space that the experiments in this study cover at

975   pressures of 50 to 120 MPa. References for the data found in Table S1.

976   Figure 2. SiO_2 versus halogen concentrations in experimental glass products, along with their

977   natural matrix glass compositions. Errors given are 1 standard deviation of the range of the

978   values measured.

979   Figure 3. Showing Cl melt contents of the experiments of Quizapu, dacite starting material

980   (green) and Kelud, basaltic andesite starting material (blue), with the corresponding modelled

981   H_2O contents from MELTS. The dashed lines indicate where brine and vapor phases appear

982   at 50 MPa and 200 MPa pressures. The crosses indicate the maximum Cl contents for each

983   experiment as modelled using Webster et al., 2015 Cl solubility model. Our experiments

984   show brine under-saturated conditions.

985   Figure 4. Mass balance calculated fluid halogen concentrations, against halogen fluid-melt

986   partitioning. Maximum accumulated errors are plotted.

987   Figure 5. Plot of natural log of fluid/melt F, Cl and Br partitioning values in this study and

988   iodine value from Bureau, 2000 against ionic radius in Angstroms. For comparison the

989   dataset and trendline from Bureau et al., (2000) is plotted.The green trendline shown is from

990   the Quizapu dataset, which represents the best correlation. Error bars indicate 1 standard

991   deviation of the values for the pressures (50-120 MPa), temperatures (800°C – 1100°C) and

992   XH2O (0.55-1) conditions. The biggest difference is the differing F partitioning values

993   (higher in this study) which alters the regression equation. The F partitioning value in Bureau

994   et al., (2000), was from Webster et al., (1992), measured in granitic melts.

995   Figure 6. Effects of glass composition (Larsen differentiation) and temperature on bulk

996   partitioning of halogens. R2 values shown above report both the unweighted and weighted

997   regressions. Variance-weighted regression was applied to Quizapu dataset which has higher

998   uncertainties (D, E and F), providing revised R2 values and the trend lines against

999   temperature plotted above.

1000   Figure 7. Scatter plot of matrices of different elements and the Cl, F and Br partitioning

1001   values, with bivariate scatter plots below the diagonal, histograms on the diagonal, and the

1002   Pearson correlation above the diagonal. The key correlations are highlighted in red. In the

1003   scatter plots the X axes represent the range of values of the element in the same row, while

1004   the Y axes represent the element in the vertical column.

1005   Figure 8. The molar Aluminium/Calcium+Sodium+Potassium ratio for data in these study as

1006   a comparison to data from literature (including CO2 bearing systems) for non-brine systems,

1007   and therefore thought to represent henrian partitioning. Literature sources in table S1 and

1008   broken down by study in figure S7.

Table 1 Experiments conducted under NNO oxygen buffer.

Experiment number	Starting material	Pressure (MPa)	Temperature °C	XH$_2$O (wt %)	Glass content (vol%)	Volatile mass (g)	Glass mass (g)	Duration (hours)
Kel14	Basaltic andesite	50	1000	1	43.9	0.0298	0.0162	49
Kel12	Basaltic andesite	50	1050	1	47.4	0.0044	0.0446	36
Kel9	Basaltic	50	1100	1	39.5	0.0131	0.0409	24

	andesite							
Kel35	Basaltic andesite	50	1050	0.55	30.1	0.0144	0.0289	46
Kel34	Basaltic andesite	50	1025	1	36.9	0.0133	0.0433	42
Kel23	Basaltic andesite	50	1000	0.56	28.7	0.0302	0.0211	48
Kel2	Basaltic andesite	100	1000	1	31.0	0.0139	0.0212	44
Kel15	Basaltic andesite	100	1100	1	43.0	0.0056	0.0448	24
Quiz5	Dacite	120	900	1	92.1	0.0455	0.0852	168
Quiz4	Dacite	120	800	1	86.5	0.0076	0.0798	170
Quiz3	Dacite	120	850	1	94.6	0.0205	0.0844	171
Quiz16	Dacite	120	900	0.5	89.0	0.0019	0.0669	167
Quiz15	Dacite	120	800	0.56	82.4	0.0092	0.0596	178
Quiz13	Dacite	120	850	0.5	86.6	0.0220	0.0585	171

1009

Table 2: Starting conditions of matrix glass and XRF data, along with Br, Cl and F contents.

wt%	Quizapu Matrix glass EMPA	Bulk rock XRF	Kelud Matrix glass EMPA	Bulk rock XRF
SiO_2	71.44	66.50	69.38	54.56
TiO_2	0.34	0.54	0.53	0.65
Al_2O_3	14.85	15.74	15.42	18.86
FeO	1.59	2.97	4.00	8.89
MnO	0.07	0.09	0.15	9.13
MgO	0.33	0.87	1.04	3.73
CaO	1.13	2.38	3.54	0.21
Na_2O	4.39	5.13	4.26	0.67
K_2O	4.02	3.27	1.74	2.79
P_2O_5		0.14	0.20	0.12
Total	98.59	97.40	100.42	99.62
SIMS (ppm)		Sigma		Sigma
F	661	44	564	56
Cl	2192	100	1476	14
Br	6.1	0.7	4.3	0.4

Bulk rock XRF from Ruprecht et al., (2012) (Quizapu) and Cassidy et al., 2019 (Kelud).

1010

1011

1012

Table 1 Experimental conditions, which were conducted under NNO oxygen buffer.

Experiment	Starting material	Pressure (MPa)	Temperature	XH2O	Glass content	Volatile mass	Glass mass	Duration (h)
Kel14	Basaltic andesite	50	1000	1	43.9	0.0298	0.0162	49
Kel12	Basaltic andesite	50	1050	1	47.4	0.0044	0.0446	36
Kel9	Basaltic andesite	50	1100	1	39.5	0.0131	0.0409	24
Kel35	Basaltic andesite	50	1050	0.55	30.1	0.0144	0.0289	46
Kel34	Basaltic andesite	50	1025	1	36.9	0.0133	0.0433	42
Kel23	Basaltic andesite	50	1000	0.56	28.7	0.0302	0.0211	48
Kel2	Basaltic andesite	100	1000	1	31.0	0.0139	0.0212	44
Kel15	Basaltic andesite	100	1100	1	43.0	0.0056	0.0448	24
Quiz5	Dacite	120	900	1	92.1	0.0455	0.0852	168
Quiz4	Dacite	120	800	1	86.5	0.0076	0.0798	170
Quiz3	Dacite	120	850	1	94.6	0.0205	0.0844	171
Quiz16	Dacite	120	900	0.5	89.0	0.0019	0.0669	167
Quiz15	Dacite	120	800	0.56	82.4	0.0092	0.0596	178
Quiz13	Dacite	120	850	0.5	86.6	0.0220	0.0585	171

hours)

Table 2: Starting conditions of matrix glass and XRF data, along with Br, Cl and F contents.

wt%	Quizapu		Kelud	
	Matrix glass	Bulk rock	Matrix glass	Bulk rock
	EMPA	XRF	EMPA	XRF
SiO2	71.44	66.50	69.38	54.56
TiO2	0.34	0.54	0.53	0.65
Al2O3	14.85	15.74	15.42	18.86
FeO	1.59	2.97	4.00	8.89
MnO	0.07	0.09	0.15	0.21
MgO	0.33	0.87	1.04	3.73
CaO	1.13	2.38	3.54	9.13
Na2O	4.39	5.13	4.26	2.79
K2O	4.02	3.27	1.74	0.67
P2O5		0.14	0.20	0.12
Total	98.59	97.40	100.42	99.62
SIMS (ppm)		Sigma		Sigma
F	661	*44*	564	*56*
Cl	2192	*100*	1476	*14*
Br	6.1	*0.7*	4.3	*0.4*

Bulk rock XRF from Ruprecht et al., (2012) (Quizapu) and Cassidy et al., 2019 (Kelud).

Table 3: Major element and Br, Cl and F contents of experiments, modelled water and CO2 values and F

| EMPA (wt%)	Kel14	Sigma	Kel12		Kel9		Kel35		Kel34
Cl	0.08	0.01	0.05	0.01	0.04	0.04	0.19	0.10	0.11
SiO2	67.57	1.24	58.41	0.86	56.64	0.93	71.70	1.87	68.83
TiO2	0.60	0.06	0.91	0.11	0.67	0.06	0.79	0.16	0.69
Al2O3	14.08	0.25	14.64	0.56	16.01	0.36	11.87	0.22	13.98
FeO	2.81	0.49	9.31	0.99	7.75	0.57	6.31	1.25	2.98
MnO	0.13	0.02	0.24	0.04	0.22	0.04	0.18	0.04	0.13
MgO	1.17	0.23	3.29	0.26	3.90	0.65	0.91	0.13	1.27
CaO	3.17	0.32	6.95	0.21	7.88	0.68	3.13	0.53	2.72
Na2O	4.94	0.15	3.44	0.21	3.28	0.18	4.22	0.14	5.01
K2O	1.77	0.12	1.03	0.07	0.80	0.09	1.67	0.27	1.72
P2O5	0.22	0.02	0.18	0.03	0.17	0.02	0.31	0.09	0.30
Total	96.62	0.25	98.53	0.40	97.40	0.67	101.34	0.73	97.82
Modelled dissolved voltailes (wt %)									
H2O	2.48		2.69		2.47		1.72		2.53
CO2	0		0		0		0.02		0
SIMS (ppm)									
F	451	17	342	33	231	24	497	108	528
DF fl/melt	0.96	0.15	4.46	2.09	4.91	1.41	1.16	0.95	0.66
Cl	1373	88	659	86	530	116	1507	220	1652
DCl fl/melt	0.75	0.04	9.66	2.12	6.05	2.30	0.73	0.16	0.02
Br	2.2	0.9	1.3	0.3	1.1	0.3	2.8	0.8	2.0
DBr fl/melt	1.85	0.80	20.26	10.82	10.38	5.87	2.33	2.01	4.88

luid/melt partitioning. The standard deviation (1 sigma) of the multiple analyses for each experiment (n=1...

Kel23		Kel2		Kel15		Quiz5		Quiz4	
0.03	0.17	*0.03*	0.09	*0.01*	0.06	*0.02*			
0.91	71.59	1.53	67.21	0.82	59.70	1.23	67.95	0.49	68.71
0.14	0.69	0.08	0.51	0.14	0.75	0.09	0.29	0.01	0.24
0.70	12.88	0.62	14.15	0.20	13.97	0.27	14.43	0.23	13.99
0.17	2.80	0.39	2.10	0.26	5.86	0.46	1.35	0.05	1.02
0.03	0.12	0.03	0.13	0.03	0.23	0.03	0.06	*0.02*	0.05
0.14	0.88	0.59	1.26	0.14	3.52	0.31	0.27	*0.01*	0.48
0.62	1.97	0.30	2.87	0.21	6.44	0.49	1.14	*0.03*	0.97
0.20	5.06	0.33	4.24	0.09	3.94	0.15	3.25	0.31	3.26
0.19	2.08	0.11	1.61	0.09	1.13	0.10	3.56	0.13	3.70
0.04	0.27	0.04	0.20	0.02	0.19	0.04	0.04	0.02	0.04
0.44	98.56	0.77	94.44	0.32	95.83	0.45	92.34	0.98	92.46
	1.59		3.68		3.79		4.35		4.35
	0.02		0		0		0		0
18	500	94	555	22	496	5	527	9	706
0.09	0.45	0.29	0.54	0.05	0.71	0.03	0.28	0.08	0.03
104	2110	409	969	35	700	4	486	5	966
0.02	0.02	0.02	1.56	0.10	8.18	0.70	5.85	0.33	12.69
0.0	1.5	0.3	2.3	0.4	1.6	0.2	1.0	0.0	1.3
0.28	2.19	0.96	2.25	0.97	13.07	3.74	8.95	1.70	36.40

1-24)

| Quiz3		Quiz16		Quiz15		Quiz13		
			0.29	0.01	0.06	0.01	0.11	0.02
1.03	66.43	0.51	69.71	0.34	68.74	1.05	68.63	0.58
0.11	0.32	0.02	0.35	0.02	0.26	0.11	0.30	0.02
0.86	15.46	0.27	14.64	0.13	15.00	1.47	14.61	0.19
0.29	1.78	0.11	1.54	0.10	1.12	0.27	1.20	0.09
0.03	0.09	*0.02*	0.07	*0.02*	0.06	*0.02*	0.06	*0.03*
0.54	0.47	*0.03*	0.35	0.02	0.18	0.18	0.26	0.02
0.34	1.67	*0.07*	1.03	*0.03*	1.19	*0.56*	1.05	*0.06*
0.59	3.82	0.11	4.47	*0.14*	4.35	*0.57*	3.93	*0.21*
0.33	3.43	0.07	3.98	0.06	3.76	0.45	3.85	0.07
0.04	0.05	0.03						
1.10	93.51	0.31	96.45	0.43	94.74	1.44	94.01	0.84
	4.36		2.24		2.92		2.36	
	0		0.05		0.03		0.05	
60	345	11	643	6	461	5	490	12
0.03		3.41	0.24	0.24	3.14	0.36	0.90	0.18
84	257	27	1578	49	652	3	495	4
2.78			11.87	1.74	16.07	0.76	9.04	0.49
0.1	0.4	0.1	3.5	0.2	0.5	0.4	0.8	0.0
8.30		70.59	23.26	9.09	69.24	36.72	18.84	2.93
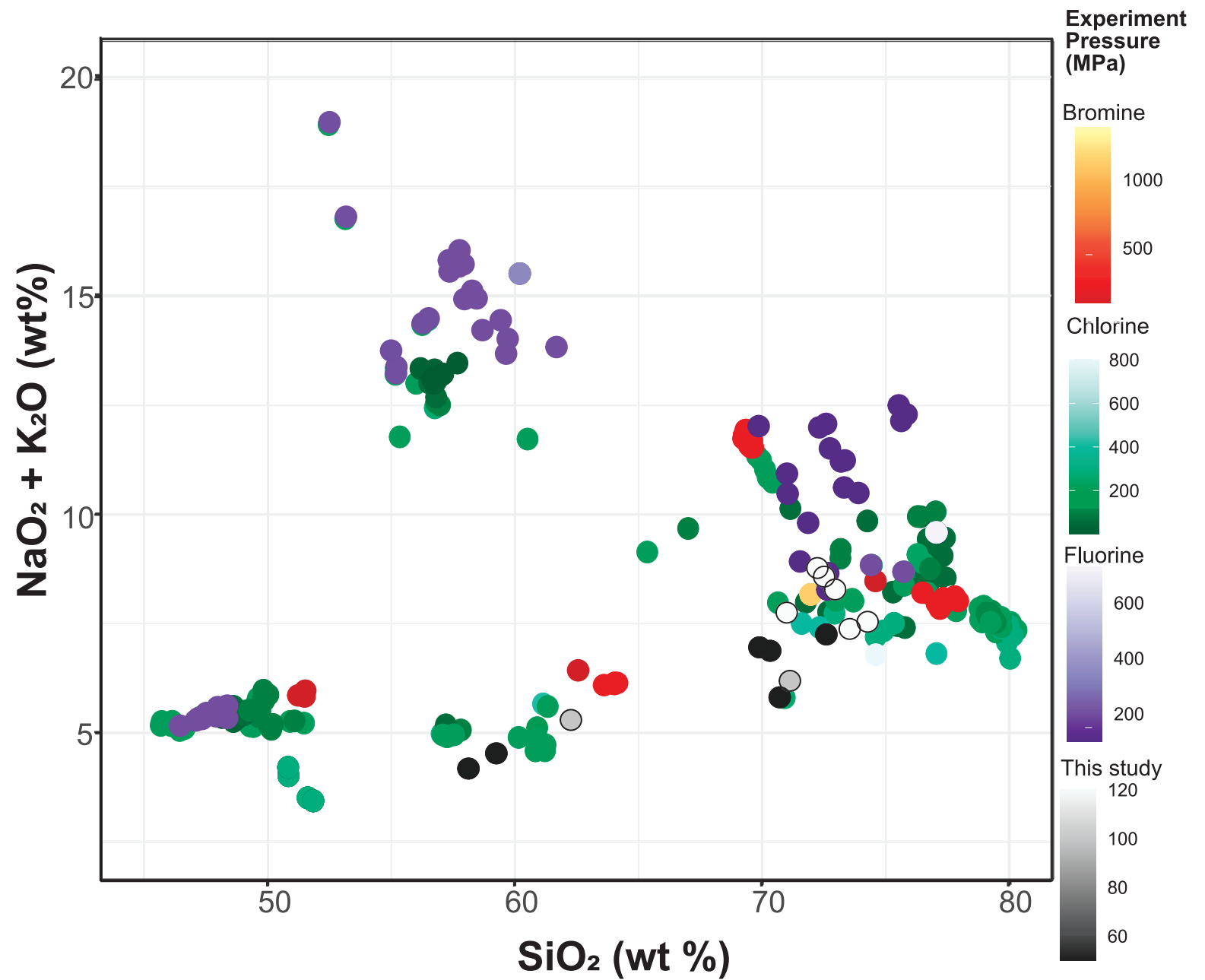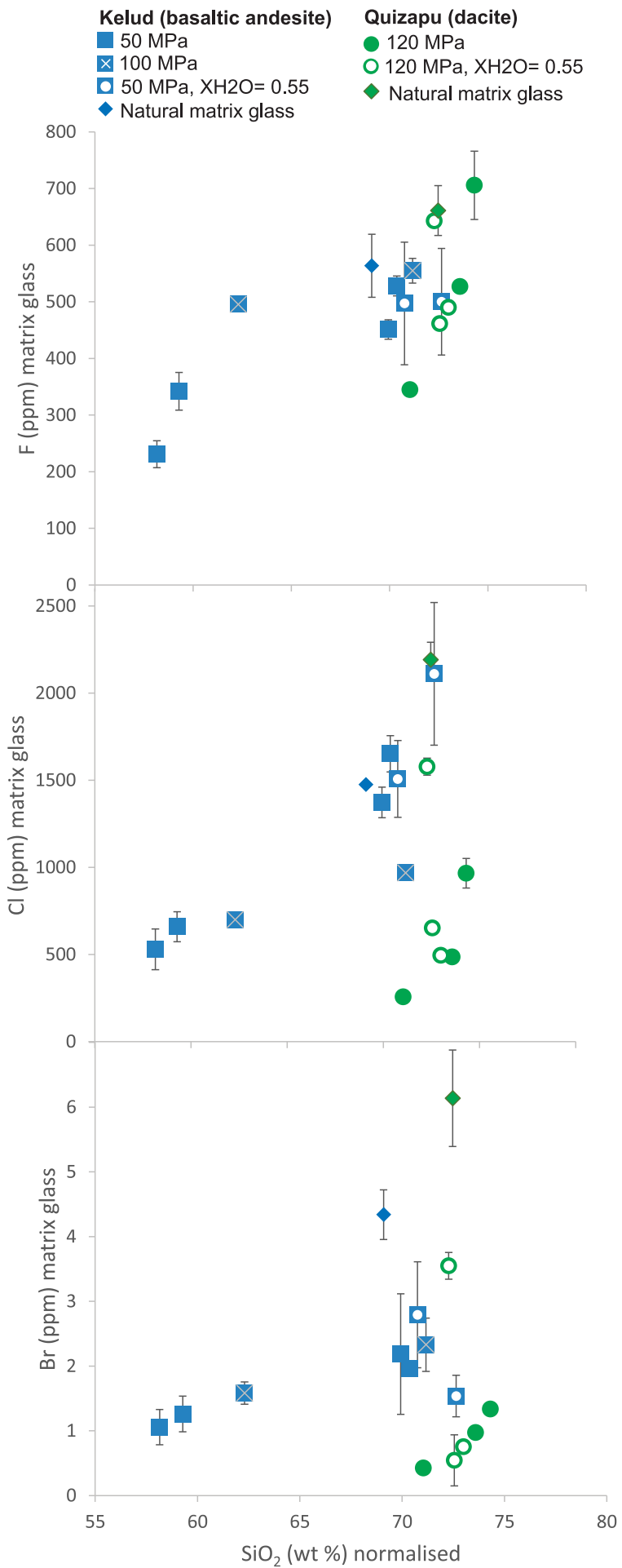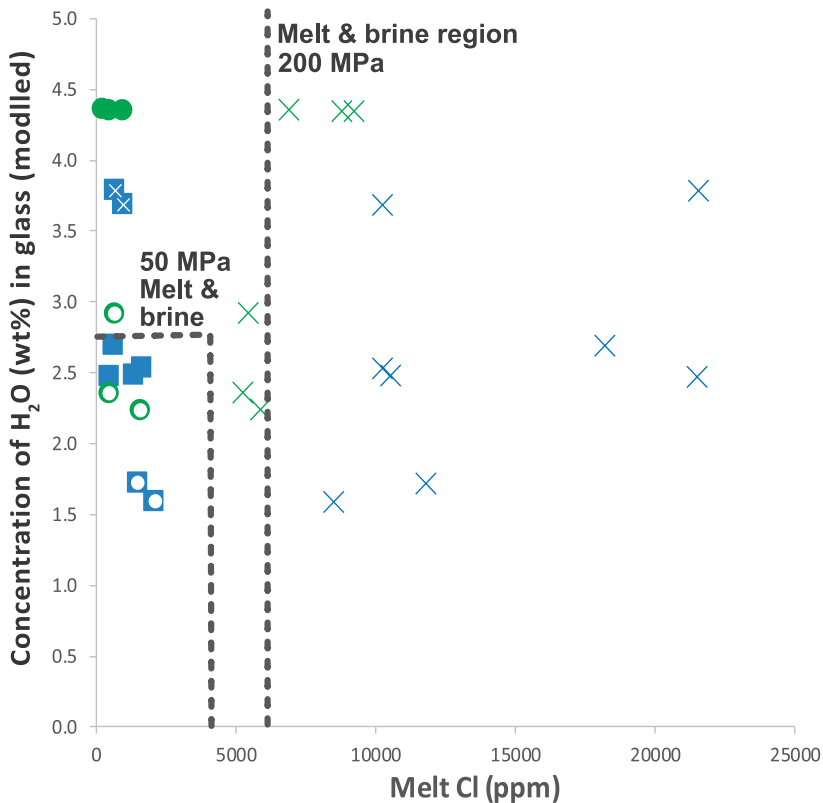
Kelud (basaltic andesite)
- 50 MPa
- 100 MPa
- 50 MPa, $XH_2O = 0.55$
- Modelled maximum Cl solubility

Quizapu (dacite)
- 120 MPa
- 120 MPa, $XH_2O = 0.55$
- Modelled maximum Cl solubility
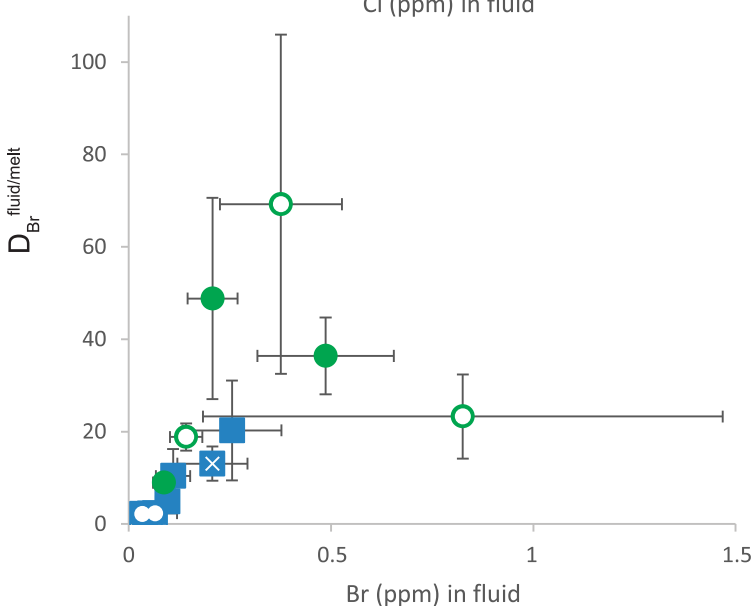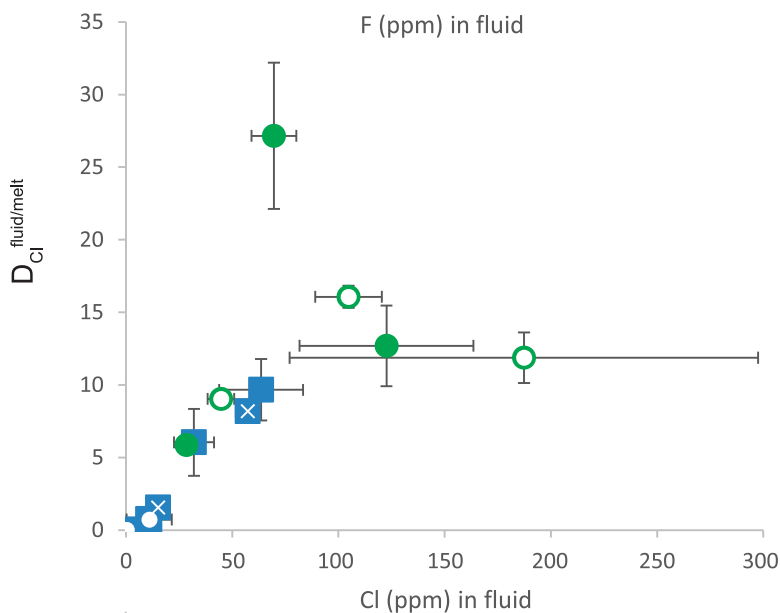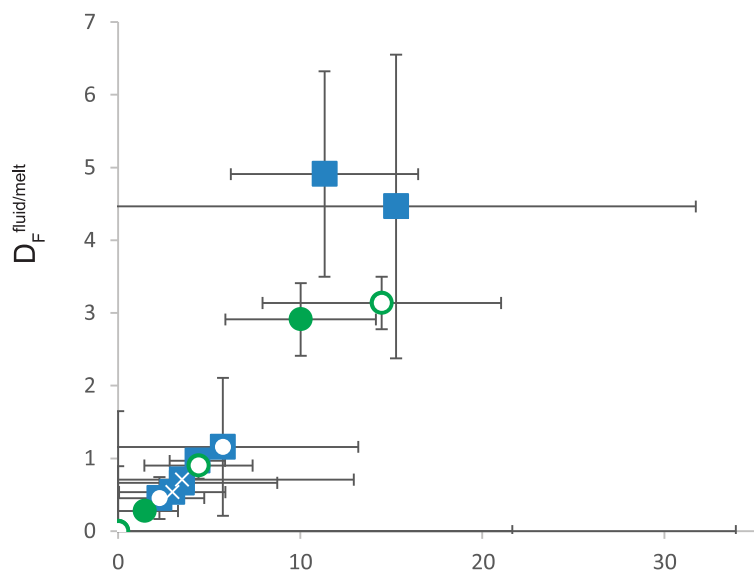
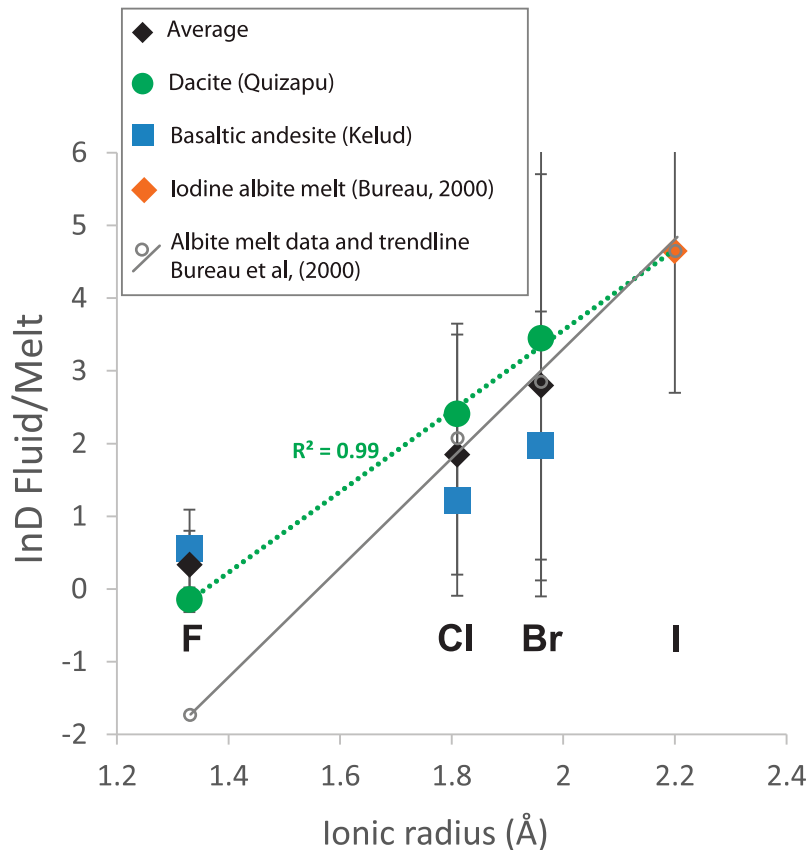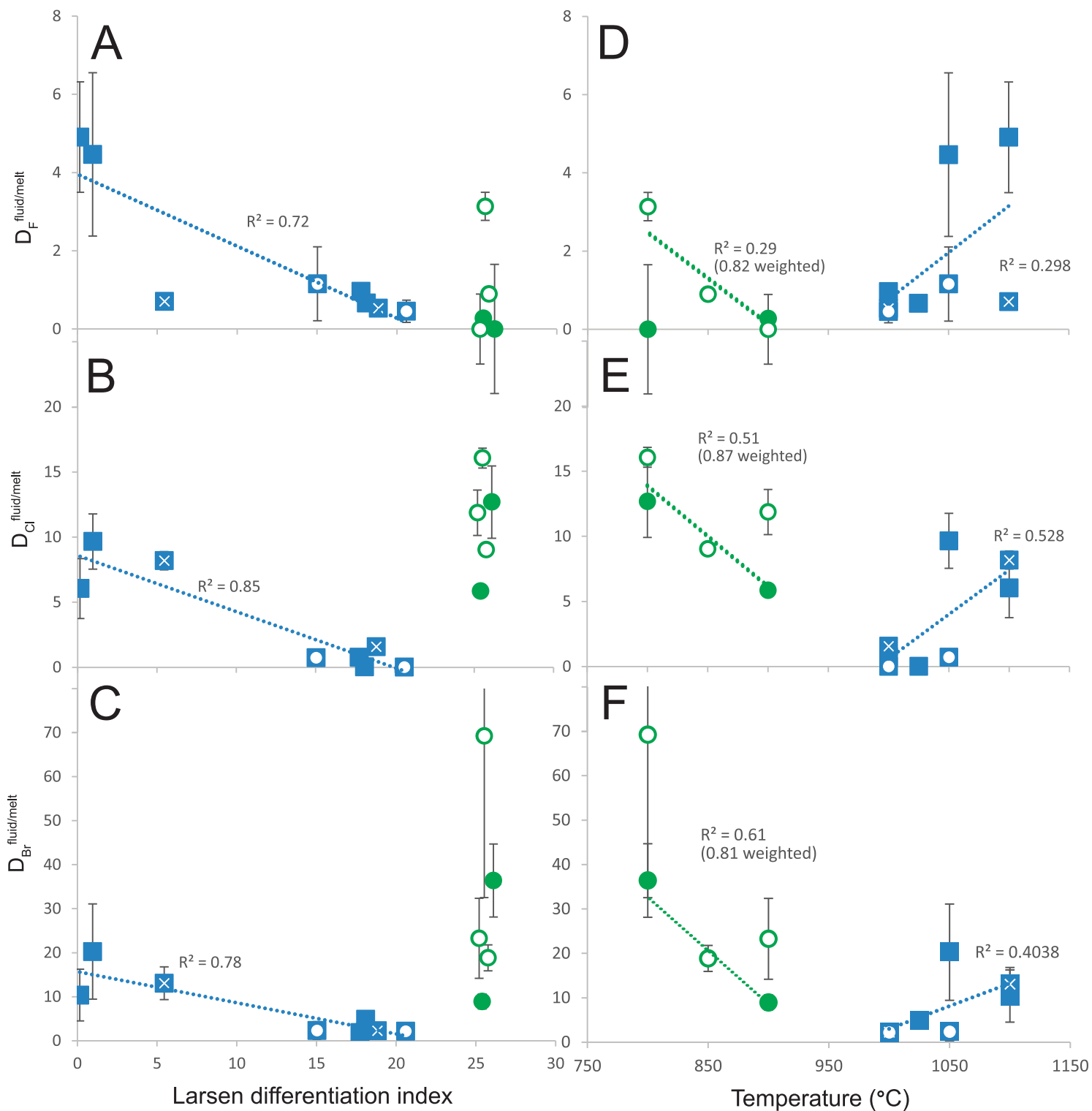**Kelud (basaltic andesite)**
- ■ 50 MPa
- ✕ 100 MPa
- ◨ 50 MPa, XH₂O= 0.55

Quizapu (dacite)
- ● 120 MPa
- ○ 120 MPa, XH₂O= 0.55

Legend:
- ◆ Average
- ● Dacite (Quizapu)
- ■ Basaltic andesite (Kelud)
- ◆ Iodine albite melt (Bureau, 2000)
- ○ Albite melt data and trendline Bureau et al, (2000)

$R^2 = 0.99$

Y-axis: lnD Fluid/Melt

X-axis: Ionic radius (Å)

Data point labels: F, Cl, Br, I

Kelud (basaltic andesite)

■ 50 MPa, $XH_2O= 1$
⊠ 100 MPa, $XH_2O= 1$
◉ 50 MPa, $XH_2O= 0.55$

Quizapu (dacite)

● 120 MPa, $XH_2O= 1$
○ 120 MPa, $XH_2O= 0.55$

Y-axes (top to bottom): $D_F^{fluid/melt}$, $D_{Cl}^{fluid/melt}$, $D_{Br}^{fluid/melt}$

X-axis: A/CNK
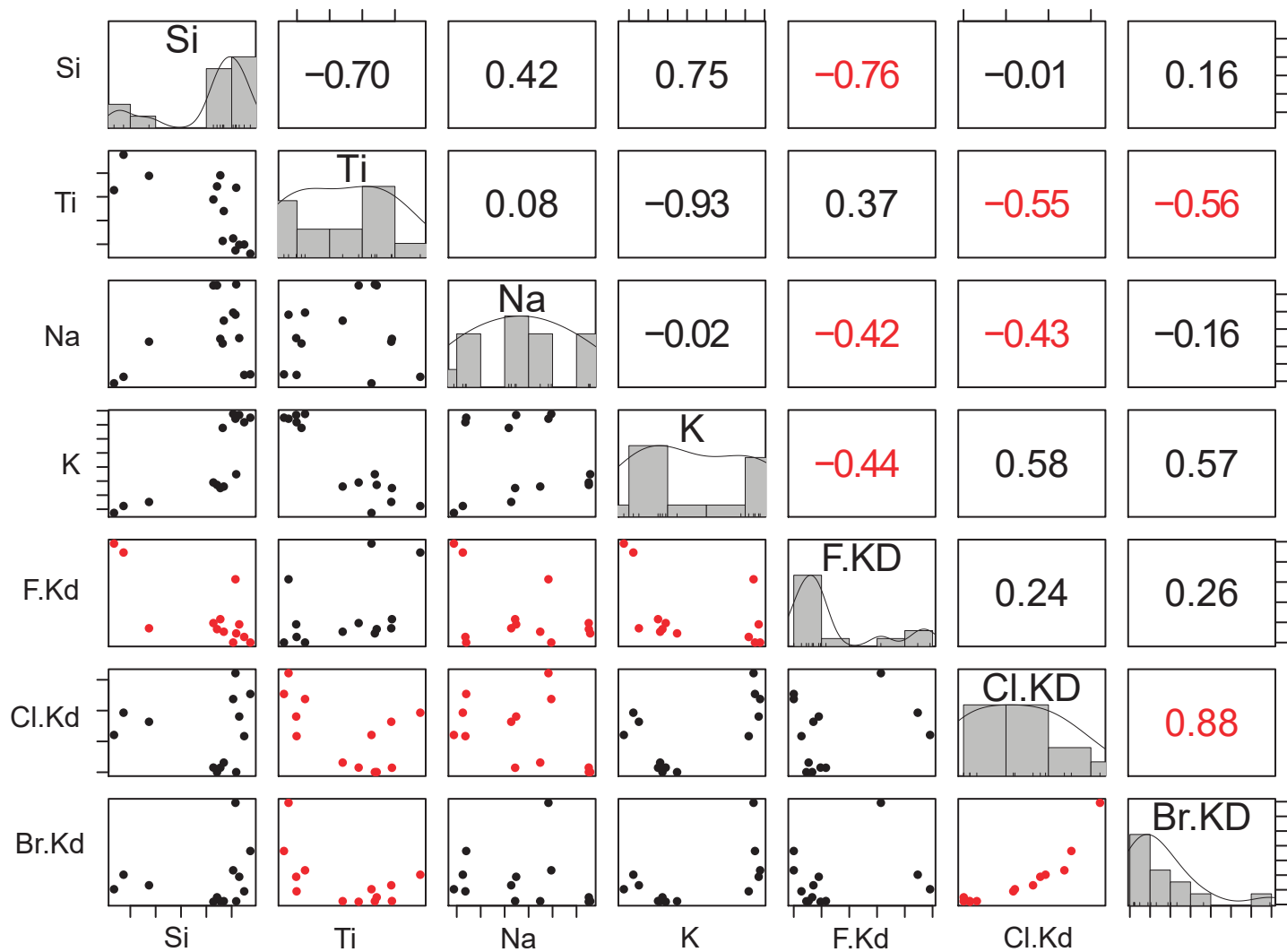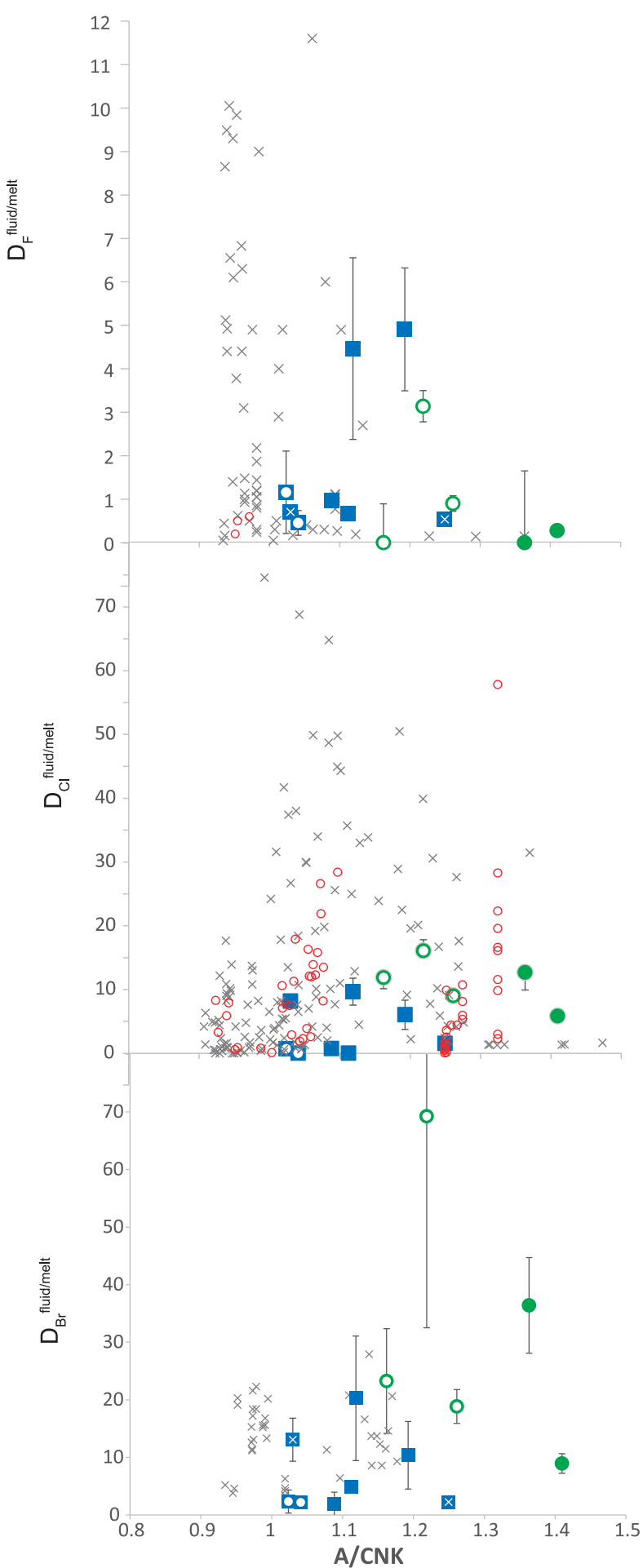
Kelud (basaltic andesite)

- ■ 50 MPa, $XH_2O = 1$
- ⊠ 100 MPa, $XH_2O = 1$
- ▣ 50 MPa, $XH_2O = 0.55$
- ✕ Literature data, $XH_2O = 1$

Quizapu (dacite)

- ● 120 MPa, $XH_2O = 1$
- ○ 120 MPa, $XH_2O = 0.55$
- ○ Literature data, $XH_2O = <1$ (CO_2 bearing)